

Snow Height Determination by Polarimetric Phase Differences in X-Band SAR Data

Silvan Leinss, *Student Member, IEEE*, Giuseppe Parrella, *Student Member, IEEE*, and Irena Hajnsek, *Fellow, IEEE*

Abstract—The copolar phase difference (CPD) between VV and HH polarization of X-band SAR acquisitions shows a significant dependence on the depth of fresh snow. Phase differences of 5–15 deg/10 cm fresh snow were determined at a frequency of 9.65 GHz by comparing spatial and temporal variations of snow depth (SD) with the CPD. Spatial correlations were derived from snow transect measurements during January 2012 and TanDEM-X acquisitions. Temporal correlations were derived from weather station data and TerraSAR-X acquisitions between December 2012 and April 2013. All measurements were done at a test field near the city Sodankylae, Finland. To explain the observed CPD, a model derives birefringent properties from the microstructure of snow, which is described as aligned elliptical particles. The microscopic description is based on computer tomography observations. Different incidence angles were analyzed in consistency with the model. The temporal evolution of the CPD was linked to the temperature-gradient-driven recrystallization process. Sudden increases in the CPD indicate fresh snow. Slow decreases indicate the subsequent recrystallization process. The background signal of wet soil was considered and causes a small negative offset to the CPD. A quantitative determination of the depth of fresh snow is possible, because the specific CPD per meter of snow can be estimated. Spatial resolutions below 100×100 m are achievable with sensors such as TerraSAR-X or TanDEM-X. This paper presents a theoretical relationship between the microstructure of snow and the CPD and relates the CPD theoretically and empirically to the depth of fresh snow.

Index Terms—Birefringence, copolar phase difference, dry snow, fresh snow, polarimetry, snow anisotropy, snow microstructure, synthetic aperture radar, TanDEM-X, TerraSAR-X, VV-HH phase difference.

I. INTRODUCTION

SNOW height detection is still a challenging topic for remote sensing techniques. Spatially, there is a strong variability in height and stratigraphy [3]–[6]. Snow density varies typically seasonally [7] but depends also on climate zones [8]. On the

Manuscript received September 30, 2013; revised March 27, 2014; accepted April 28, 2014. Date of publication June 19, 2014; date of current version November 04, 2014. The *in situ* data collection was supported by the European Space Agency activity “Technical assistance for the deployment of an X- to Ku-band scatterometer during the NoSREx-III experiment” (ESA ESTEC Contract no. 22671/09/NL/JA/ef) [46].

S. Leinss is with the Institute of Environmental Engineering, Swiss Federal Institute of Technology in Zurich (ETH), 8093 Zürich, Switzerland (e-mail: leinss@ifu.baug.ethz.ch).

G. Parrella is with the Microwaves and Radar Institute, German Aerospace Center (DLR), Wessling 82234, Germany (e-mail: giuseppe.parrella@dlr.de).

I. Hajnsek is with the Institute of Environmental Engineering, Swiss Federal Institute of Technology in Zurich (ETH), 8093 Zürich, Switzerland, and also with the Microwaves and Radar Institute, German Aerospace Center (DLR), Wessling 82234, Germany (e-mail: hajnsek@ifu.baug.ethz.ch; irena.hajnsek@dlr.de).

Color versions of one or more of the figures in this paper are available online at <http://ieeexplore.ieee.org>.

Digital Object Identifier 10.1109/JSTARS.2014.2323199

microscopic scale, grain size, grain form, and even crystal orientation vary with depth and time [1], [9]. Active radar sensors, especially synthetic aperture radar (SAR) systems are of high interest, as they show a sensitivity to snow volume with a resolution on the meter scale. Numerous works have been published using backscatter signals at all available frequencies and polarizations. For snow, the backscatter coefficient was already measured in 1977 [10] and was modeled for various frequencies, layers, and polarizations [11]. It was shown that only very high frequencies at Ku-band or higher have a reasonable dependence on SD or on the snow water equivalent (SWE) of dry snow [12]–[17]. Frequencies at X-band or below penetrate through dry snow such that the main backscatter contributions arise from the frozen soil below. For a transitional range between dry and wet snow ($0.1\% < m_v < 0.5\%$), the dominant backscattering can occur in the volume; however, for wet snow ($m_v > 2\%$), scattering occurs only in the top few centimeters of the surface [18], [19]. Water with its high dielectric constant changes the dielectric properties of snow by orders of magnitude, resulting in a very small penetration depth caused by absorption and reflection [19]–[22]. The effect that backscattering from a smooth wet surface is much lower than from rough ground was used to detect wet snow and to predict melt water runoff [23]–[26]. Algorithms based on the polarimetric backscatter signal were developed and used for snow wetness and snow density determination [27], [28].

The phase of the backscattered electromagnetic field, included into the analysis, enhanced the pure imaging capability of active radar systems. Coherent decomposition methods, based on a H/A/ $\bar{\alpha}$ -analysis, can be used to classify wet and dry snow [29]–[31]. Interferometric methods have opened new approaches, which are sensitive to snow cover and which are all based on the complex-valued correlation function between two SAR-scenes, the interferometric coherence γ . Using (multipass) DInSAR techniques, the magnitude of γ at L-band was maintained between October and April but was lost for wet snow covered areas [32]. At C- and X-band, snowfall, snow metamorphosis, and densification lead to a quick loss of γ within a few days [33]. When γ is high enough, the phase difference caused by the signal delay of snow can be analyzed [34]–[36]. However, local deformations, soil freezing, soil moisture, atmospheric effects, and even just rough soil [37] can impede a successful SD estimation [38]. The summer–winter comparison of InSAR derived digital surface models requires high frequencies, large baselines and is only possible when snow is wet and scattering occurs at the snow surface [39]. For dry snow and frequencies below 10–15 GHz, volume scattering within the shallow seasonal snow cover is typically too low to cause any significant

volume decorrelation, as it would be required for the RVoG-model [40]. However, the depth of many meters of multiyear snow was estimated by means of volume decorrelation [41].

Polarimetric methods which consider the copolar phase difference (CPD) between VV and HH polarization are not applied very much despite the fact that in weather radars the use of the CPD is known and depends on the oblate shape of snow or rain particles [42], [43]. The anisotropic structure of snow was already studied in a ground-based experiment where the CPD changed by up to 150° after 15 cm of fresh snow at a frequency of 95 GHz. The author provides a theoretical model to explain the observed CPD. The model is based on observed horizontally aligned structures in snow samples, which were taken at the experiment site [44]. The anisotropic structure of snow was confirmed in recent measurements of the Swiss Institute for Snow and Avalanche Research (SLF). The temporal evolution of the microstructure of snow samples were analyzed by computer tomographic measurements with a resolution of 25 μm . It was found that snow changes its structure from horizontally to vertically aligned ice grains [2]. The driving force for snow metamorphism is a vertical temperature gradient [9]. A general treatment to determine the anisotropy of snow and to derive the conductivity tensor by means of second-order correlation functions is provided [45] with the comment that the anisotropy has a strong effect on thermal conductivity, but only a minor influence on dielectric properties. However, an analysis of phase-differences in the polarimetric SAR signal allows to detect these minor changes in the dielectric tensor.

This paper derives a theoretical relationship between the microstructure of snow and the CPD between VV and HH polarization. Observed phase differences are theoretically and empirically related to the measured depth of fresh fallen snow. Large sets of spatially and temporally distributed ground measurements are available from field campaigns and weather stations. They form a good basis for comparison with spaceborne SAR-data from the satellites TerraSAR-X and TanDEM-X. The paper is organized as follows: Section II describes specific properties of the test site, the radar acquisitions, the meteorological conditions, and the ground data. Section III specifies the physical properties of snow, explains reasons for CPDs, and presents a theoretical model based on the microstructure of snow. Section IV shows a relationship between fresh snow and the CPD by the analysis of time-series data. The processing of spatially distributed ground data is described in Section V and Section VI contains the data analysis and discussion of the spatially distributed results. Section VII summarizes the results and gives suggestions for future experiments.

II. EXPERIMENTAL DATA

A. Test Site

Within the framework of the ESA Earth Explorer Mission CoReH2O, a super test and validation site was established to conduct the Nordic Snow Radar Experiment (NoSREx) campaigns [46]. Different snow- and permafrost-related experiments were conducted, on the ground, from air and from space. The test site is located in northern Finland, a few kilometers south-east

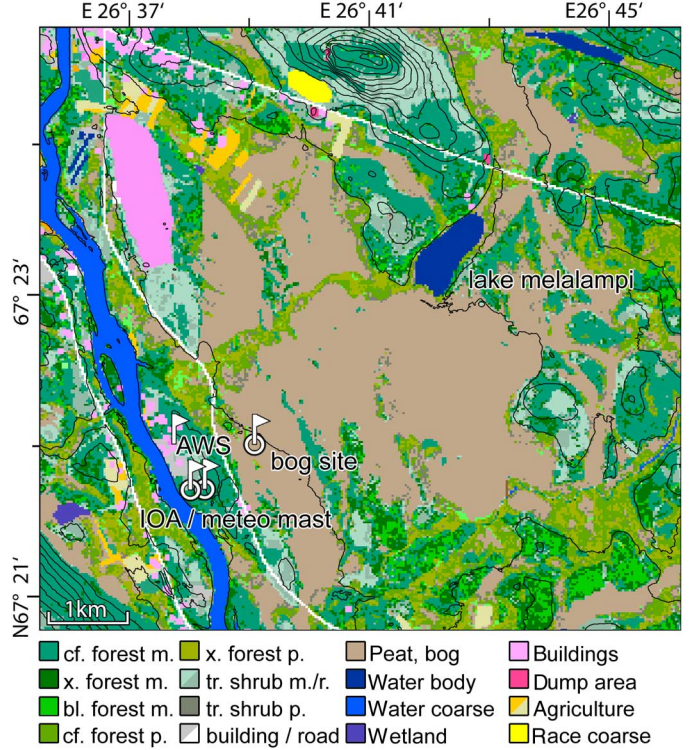


Fig. 1. Land cover classification map (CLC 2006). Forest classification: cf., conifer; x., mixed; bl., broad leaved; tr. shrub, transitional shrub. Soil types: p., peat; m., mineral soil. Contour lines with an interval of 5 m show the topography. Flags mark the location of ground measurement stations: AWS, automatic weather station; IOA, intensive observation area; meteo mast, meteorological mast; bog site. Meteorological data from the stations are shown in Figs. 3 and 4.

from the town Sodankylae. Fig. 1 shows the 25-m resolution Corine Land Cover (CLC) map (2006) together with 5 m contour lines. The dominant types of land cover are bogs and peat surrounded by conifer and mixed forest. The 12-km² large bog area differs by only 2 m from the mean height of 183 m above the sea level. Surrounding hills, which rise a few meters above the bog area, are mainly covered with forest and shrub on mineral soil.

B. SAR Acquisitions

Dual-pol X-band SAR acquisitions in HH and VV polarization were taken during two winters, 2011/2012 and 2012/2013. In the first winter, bistatic data from the TanDEM-X formation (TDM) were acquired, which provides two acquisitions per polarization, one from each satellite, TanDEM-X (TDX), and TerraSAR-X (TSX). The scenes were acquired using the standard stripmap mode with a resolution of 1.4–2.1 m in range and 2.3–3.1 m in azimuth. Acquisitions from three different orbits with different incidence angles were analyzed. Additionally, a full time series of VV/VH-polarized TSX acquisitions with 11 days repeat time and an incidence angle of $\theta = 33.8^\circ$ was analyzed to get information about the temporal evolution of the backscatter signal σ_0 . To establish a better data basis and to verify the observed relationship between snow height and CPD during the winter 2011/2012, a full time series of dual-pol TSX acquisitions (HH/VV) including a few TDM acquisitions were taken during the winter 2012/2013. Additionally, a full time series of VV/VH-polarized TSX acquisitions was acquired again. Table I

TABLE I
LIST OF ANALYZED TDM AND TSX ACQUISITIONS

Date (yyyy-mm-dd)	Time (h)	aoi θ	Orbit
TDM acquisitions, HH/VV:			
2011-11-04	15:30	32.7°	130 asc
2012-01-03	04:47	41.5°	32 desc
2012-01-03	15:39	39.7°	39 asc
2012-01-09	15:30	32.7°	130 asc
2012-01-14	04:47	41.5°	32 desc
2012-01-14	15:39	39.7°	39 asc
2012-01-25	04:47	41.5°	32 desc
2012-02-16	15:39	39.7°	39 asc
2012-03-26	15:30	32.7°	130 asc
2012-04-28	15:30	32.7°	130 asc
2012-04-20	15:30	32.7°	130 asc
2012-10-10	15:30	32.7°	130 asc
2012-10-21	15:30	32.7°	130 asc
2012-11-01	15:30	32.7°	130 asc
2013-03-13	15:30	32.7°	130 asc
2013-03-24	15:30	32.7°	130 asc
TSX acquisitions, HH/VV:			
2012-11-23 – 2013-06-09 (every 11 days)	15:30	32.7°	130 asc
TSX acquisitions, VV/VH:			
2011-10-01 – 2012-05-30	04:55	33.8°	108 desc
2012-10-09 – 2013-06-30 (both winters every 11 days)	04:55	33.8°	108 desc

aoi, angle of incidence.

shows a list of all acquisitions. The radar backscatter image of the test site is shown for November 2011 and January 2012 as a false-color composition in Fig. 2. The images show a strong difference in backscatter signal between peatland and forest in January, which does not exist in November. The difference is explained by very low backscattering from wet soil under thin ice in January.

C. Ground Measurements

A wealth of ground measurements is available from automatic measurement stations (Fig. 1 shows locations). An automatic weather station (AWS) measured air temperature, SD, and other meteorological data once per minute. About 600 m south-east is the “Intensive Observation Area” (IOA) where soil temperature and soil moisture were measured every 10 min. Located next to the IOA, the meteorological mast (meteo mast) measured soil and snow temperature profiles with a 10-min interval. One kilometer east of the AWS, at the “bog site”, soil temperature and SD were measured every 10 min by an AWS. Snow pit profiles were analyzed every seven to ten days at the IOA and the bog site. For each snow profile, snow temperature, grain size, stratigraphical measurements, snow classification, humidity, and conductivity were determined. SD was measured between the IOA and the bog site every 100 m along a 4-km long transect “snow course” (sc) to determine the SD on different land cover types, mainly forest and bog. SD was measured every meter for 21 points on a forest opening close to the AWS at the “snow variability coarse” (svc) (for data, see Fig. 3). SD was measured along a few kilometers long transects with a spacing of 10–100 m on the peatland and in the forests, which are shown in Fig. 1. The transects were acquired during 20 extended field campaigns in the winter 2011/2012 (see Table II). The measurements were done by

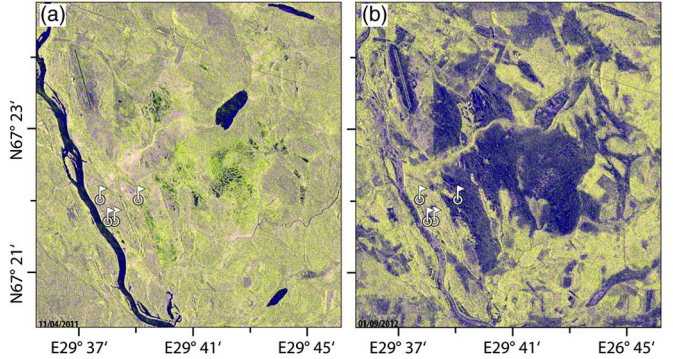


Fig. 2. False color composition with channels: red, HH; green, VV; and blue, $|HH - VV|$ from November 4, 2011 (a) and January 9, 2012 (b). The backscatter signal of the bog area is reduced for both polarizations (HH and VV) during winter (b) compared to autumn (a) and allows a clear separation from forests which keep a strong backscattering during winter. The position of ground measurement stations are marked like in Fig. 1.

TABLE II
LIST OF CAMPAIGNS WITH SD TRANSECT MEASUREMENTS

Campaign date (yyyy-mm-dd)	SD samples per transect (separated by commas)	Mean SD (cm) \pm stddev.
2011-12-19	426, 61, 62, 40	25 ± 06
2011-12-20	18	37 ± 14
2012-01-09	561, 46, 62, 46	31 ± 11
2012-01-10	273	12 ± 05
2012-01-23	83, 597, 34, 71, 46	34 ± 16
2012-01-24	423, 40, 25	46 ± 08
2012-02-07	164, 352	48 ± 10
2012-02-08	178, 358, 88	37 ± 16
2012-02-09	49, 36	47 ± 10
2012-02-22	440, 1293, 66, 44, 38, 115, 1221	55 ± 21
2012-02-23	1627, 348, 36, 8	68 ± 13
2012-02-24	1205	63 ± 10
2012-02-25	884, 2725	53 ± 10
2012-02-26	571, 9, 61, 61	60 ± 13
2012-02-29	2872, 47, 13, 857	51 ± 28
2012-03-01	1200, 663, 67, 51, 32, 931	63 ± 10
2012-03-05	55, 60	57 ± 14
2012-03-08	384, 51, 65	61 ± 12
2012-03-23	60, 63, 64, 21	51 ± 23

traditional means using an aluminum pole (avalanche probe) and a hand-held GPS and with a self-recording GPS SD probe [47]. All ground campaigns were organized by the Finnish Meteorological Institute (FMI).

Weather conditions, especially the vertical temperature gradient within the snow volume, have an important influence on the snow structure and the recrystallization speed of ice grains [9], [48], [49]. Therefore, weather conditions are summarized for both winters with respect to Figs. 3 and 4: the early season of the winter 2011/2012 was characterized by very mild temperatures. Snowfall started at the mid of November and accumulated up to 30–45 cm in January. Small temperature gradients in the snow pack caused only weak depth hoar formation in December and preserved the original structure of fresh snow. The whole snow volume is assumed to consist of one or more anisotropic layers, which contain horizontally elongated particles as it was shown for fresh snow [1], [9]. In the bog area, soil freezing happened very slowly with possibly residual free water in the top layer of the soil [46]. The mineral soil at the IOA froze already in early December. At the end of January, temperatures dropped for more

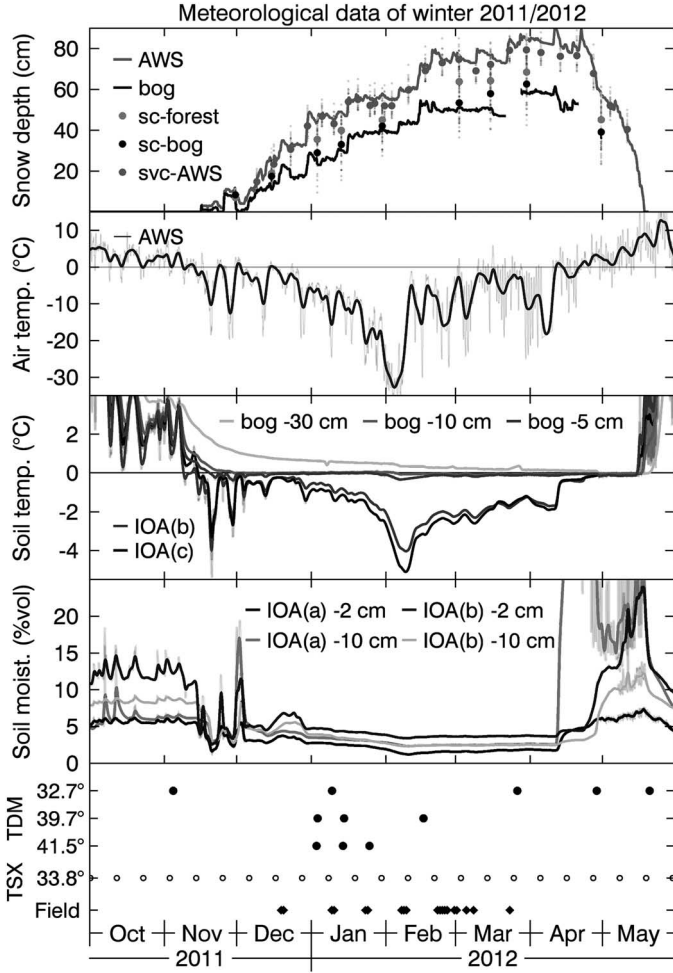


Fig. 3. Meteorological data 2011/2012: the legend indicates the data source as described in Section II-C and shown in Fig. 1. Air temperatures were smoothed with a 2-day Gaussian smoothing window (FWHM), soil temperature, and soil moisture with a 1-day window and SD with a 6-h window. The not smoothed data are shown in the background. In the topmost plot, SD values from the snow course (sc) and the snow variability course (svc) are shown as small dots to give a number about the variability of SD. Their mean values for the two land types bog and forest are shown as bullets. The soil temperature was measured 2 cm below the surface at the IOA and 5, 10 and 30 cm below surface at the bog site. The filled bullets in the undermost graph indicate the date of the TDM acquisitions. Open bullets show the TSX acquisition in VV/VH polarization. The incidence angle is given on the y-axis. The date of the field campaigns is shown as diamonds.

than 2 weeks below -15°C with temperatures below -30°C for a few days, such that strong temperature gradients of up to $45 - 80 \text{ K/m}$ occurred within the snow pack. Consequently, a fast snow recrystallization into spherical or even vertically elongated structures can be expected. Snowfall accumulated up to 60–80 cm until the end of April when snow melt started and first positive temperatures were measured during night.

The winter 2012/2013 was characterized by four major snowfalls and lower temperatures during December. The first snow melted already at the end of November before air temperatures dropped down to -15°C and the soil froze. The second happened during the first 2 weeks of December and the third occurred at the end of December. Both brought 20 cm of fresh snow. At the end of January, 30 cm snow fell within 10 days. From December to March, air temperatures varied between -5°C and -20°C . Therefore, the original structure of early winter snow was not

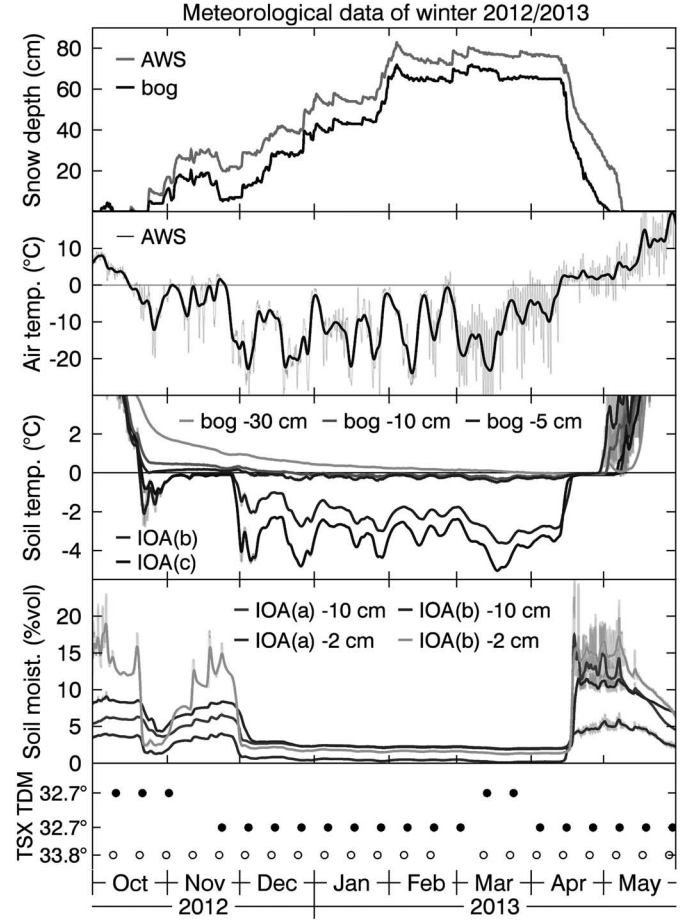


Fig. 4. Meteorological data 2012/2013: most of the data is described in the caption of Fig. 3. The filled bullets in the undermost graph indicate the dates of the TDM and TSX acquisitions in HH/VV polarization. Open bullets show the TSX acquisitions in VV/VH polarization.

preserved due to temperature gradient driven recrystallization. The soil at the IOA was well frozen during the whole winter. Soil temperatures at the bog site were only slightly below freezing point. During the whole winter, the initial difference of about 12 cm in SD between the bog and the IOA site was maintained, which suggests that the soil at the bog site was frozen and did not cause any additional snow melt.

III. THEORY AND MODEL

A. Dielectric Properties of Snow

The dielectric properties of snow at 9.65 GHz vary significantly with liquid water volume fraction m_v [19] such that three main scattering regimes can be identified. 1) Wet snow ($m_v > 2\%$) can be considered as a surface, because all reflection occurs at the snow surface due to a very low penetration. 2) Humid snow ($0.1\% < m_v < 0.5\%$), where the penetration depth δ is on the scale of the SD, acts as a good microwave absorber [20], [50]. When enough inhomogeneities of scale d are contained, which are not much smaller than the wavelength λ of the sensor ($d \gtrsim \lambda$), volume scattering can occur. Inhomogeneities could be very large ice grains, ice lenses or vertical refrozen structures. For mm-sized ice grains, absorption predominate scattering [51], [52]. 3) Dry snow can be considered as a

homogeneous, nonscattering, nonabsorbing volume, as long as no large inhomogeneities are contained. The effective dielectric constant depends mainly on the volume ratio between ice and air and their relative permittivities [53]. Consequently, the main backscatter signal results from the underlying ground, but is delayed by the refraction index of dry snow.

B. Polarimetry of an Anisotropic Medium Over Ground

A polarimetric SAR system uses polarized radar echoes to gain information about the specific scattering mechanism, which characterizes a certain target [54]. A coherent analysis, which considers the phase of different polarimetric channels, allows to distinguish between several scattering mechanisms. In this paper, the CPD between the two channels VV and HH is investigated and is defined as

$$\phi_c = \phi_{VV} - \phi_{HH} \quad (1)$$

in the backscattering alignment convention. With reference to the classical theory of polarimetry [54], three main scattering mechanisms are classified by means of ϕ_c [55]–[57]: 1) surface ($\phi_c = 0$); 2) dihedral ($\phi_c = \pi$); and 3) volume scattering where ϕ_c is uniformly distributed between $-\pi$ and π . For an arbitrary target, ϕ_c can be described by a superposition of the three scattering mechanisms. Some authors use an opposite sign convention and define the CPD as $\phi_{HH} - \phi_{VV}$. Others consider only absolute values $|\phi_c|$. Here, the definition (1) is used, mainly, to keep the measured phase differences for fresh snow positive. Co-cross-polar phase differences (e.g., $\phi_{VV} - \phi_{VH}$) are not further considered as the cross-pol phase does not give insight into the dielectrically anisotropic structure of a target.

The polarimetric signature of a surface is not affected when the surface is covered by a homogeneous, isotropic, and transparent medium. Still, some signal delay occurs caused by the refractive index of the medium. When the covering medium has an anisotropic structure, the signal delay becomes polarization-dependent and affects the polarimetric analysis. The dielectric constant ε of the medium must be treated as a dielectric tensor $\bar{\varepsilon}$ [45]. The total (one way) CPD $\Delta\phi$ after traveling through a birefringent medium depends on the specific birefringence Δn , the thickness l , and the vacuum wavelength λ

$$\Delta\phi = 2\pi l/\lambda \cdot \Delta n. \quad (2)$$

This equation is only valid for homogeneous media where no volume scattering occurs. With increasing volume scattering, the equation becomes more complex but still serves as an upper bound for the expected phase difference of a weakly inhomogeneous medium. Additionally, the copolar coherence γ_c will decrease due to volume decorrelation. The effective scattering center will move toward the upper surface, as the target is not solely defined by the surface under the transparent medium any more. For a strongly inhomogeneous medium or if the depth of the scattering center is polarization-dependent, the phase of the signal will be determined by different scatterers for each polarization. The coherent sum of all scatterers within one SAR resolution cell would lead to completely independent phases between VV and HH polarization and would, therefore, destroy the copolar coherence. In this case, the depth of

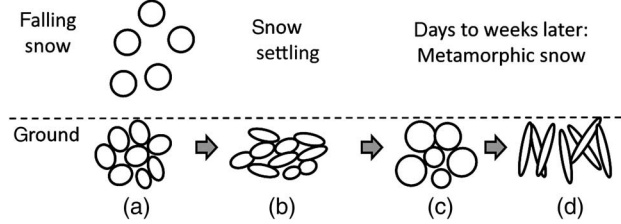


Fig. 5. Snow compresses by weight immediately after deposition. A few days to weeks later, recrystallization forms first spherical and later vertically extended ice grains, which increase in size by time: (a) random; (b) horizontally aligned; (c) isotropic; and (d) vertically aligned.

polarization-dependent scattering centers can only be measured by Pol-InSAR methods [40].

The data, which are presented in this paper, show very high coherence values γ_c . Therefore, different depths of scattering centers can be excluded and it is assumed that most of the scattering occurs at the underlying ground.

C. Anisotropic Microstructure of Snow

Fresh snow accumulates as a randomly structured medium in which the scale of heterogeneities (ice and air inclusions) are smaller than the wavelength of X-band. The fresh snow volume is compressed by its own weight (settling). The initially isotropic random structure transforms into a medium with an anisotropic, horizontally aligned structure, which recrystallizes gradually into an isotropic or even vertically aligned anisotropic structure (Fig. 5). Aligned by gravity as well as by aerodynamics while falling, snow flakes can even deposit horizontally arranged inherently.

Computer tomographic measurements at SLF reveal that snowflakes within a natural snow sample were indeed preferentially horizontally arranged at the begin of their experiment with fresh snow [2]. Four weeks after the start of the experiment, the initial structure dissolved completely and a complete recrystallization to spherical particles occurred. After 12.5 weeks, larger spherical crystals formed with well-defined local chain-like structures in the vertical direction [2]. The transformation process is driven by a vertical temperature gradient. Water molecules at the top of ice grains evaporate and deposit at the bottom of grains a few millimeters higher [9]. This process forms the vertically aligned depth hoar and firn structures which were already observed by [58].

The anisotropic structure influences the thermal conductivity, but also the dielectric properties of snow [45]. Different definitions and methods exist to determine anisotropy parameters of a medium. The “degree of anisotropy” is derived from three-dimensional computer tomographic scans [59] and was used for snow structure characterization [1]. The microstructural parameter Q can be calculated from a heterogeneous structure via two-point correlation functions [45] and is related to the aspect ratio a/b of spheroids ([45, eq. (4)] and [60, Fig. 7]). Both methods require sophisticated equipment and analysis methods. As the thermal conductivity of snow is related to the anisotropic structure [61], heat-conductivity measurements might give a good approximation for the anisotropy. Referring to this paper, the polarization-dependent propagation speed of microwaves measured by CPD might provide a new method to determine the anisotropy.

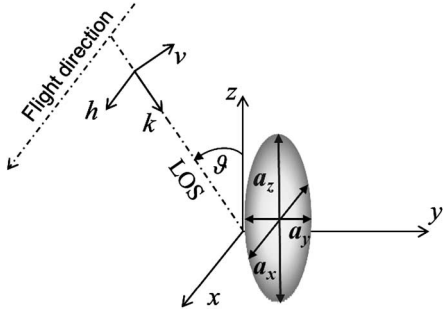


Fig. 6. Orientation of a single vertically aligned prolate particle (here, an ice grain) in the specified Cartesian coordinate system (x, y, z) and link to the radar reference frame (h, k, v) [62] in the back scattering alignment convention. k indicates the propagation vector of the incident waves and θ the incidence angle. The shown prolate particle has a length a_z and width of $a_x = a_y$ and a horizontal-to-vertical-ratio a_x/a_z smaller than one.

D. Model for the Dielectric Anisotropy of Snow

To derive the macroscopic dielectric properties from the microstructure of snow, the method proposed in [62] is adopted. The author presents an electromagnetic model based on the Maxwell Garnett theory [63] with the attempt to provide an interpretation of the polarimetric signatures of a subpolar ice cap for different frequencies, polarizations, and incidence angles. The results show that the anisotropic nature of firn could be a possible explanation for the observed CPD at L- and P-band. Beside other scattering components, the model describes the complete covariance matrix of a volume, which is populated by vertically aligned (prolate) spheroidal ice grains embedded in air. The below paragraph describes details of the model.

A single spheroidal particle can be characterized by three orthogonal dipoles, whose lengths a_x , a_y , and a_z are the axes of the spheroid along the x -, y -, and z -axes of a fixed Cartesian coordinate system (Fig. 6). The horizontal-to-vertical axes ratio a_x/a_z defines the shape of the spheroid, assuming that $a_x = a_y$. Ratios higher than one refer to horizontally oriented oblates, with longer horizontal axes a_x and a_y than a_z . Contrarily, ratios lower than 1 ($a_z > a_x$, a_y) indicate vertically oriented prolates. The special case of spherical particles is obtained for a horizontal-to-vertical ratio equal to 1 ($a_z = a_x = a_y$). By fixing a particle shape, the three depolarization factors N_i with $i \in \{x, y, z\}$ of a single spheroid can be computed by integration over s as described in [53]

$$N_i = \frac{a_x a_y a_z}{2} \int_0^\infty \frac{ds}{(s + a_i^2) \sqrt{(s + a_x^2)(s + a_y^2)(s + a_z^2)}}. \quad (3)$$

Considering air as a medium of permittivity ϵ_{air} populated by aligned spheroidal ice particles of permittivity ϵ_{ice} , the effective permittivity of the mixture is anisotropic. Along the three main directions (x, y, z), it can be written as

$$\epsilon_{\text{eff},i} = \epsilon_{\text{air}} + \mu \cdot \epsilon_{\text{air}} \cdot \frac{\epsilon_{\text{ice}} - \epsilon_{\text{air}}}{\epsilon_{\text{air}} + (1 - \mu) N_i (\epsilon_{\text{ice}} - \epsilon_{\text{air}})}. \quad (4)$$

The particle volume fraction μ is based on the snow/ice density and $i \in \{x, y, z\}$. The elements of the effective permittivity are projected onto the h - and v -axes of the radar reference frame to

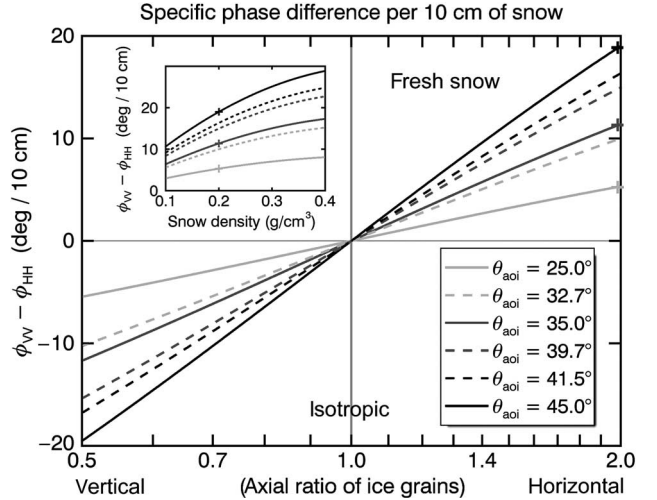


Fig. 7. Modeled CPD (y-axis) for the example of a 10-cm-thick snow layer as a function of the axial ratio of oriented, nonspherical ice grains. Snow density was set to 0.2 g/cm³. Fresh snow contains horizontal structures (axial ratio larger than one) and metamorphic snow like firn or depth hoar contains spherical or vertically aligned structures (axial ratio less than one). Dashed lines represent the expected specific phase differences for the incidence angles θ_{aoi} of the three acquisitions. The inset shows the variation of the CPD depending on snow density for horizontally aligned oblate snow particles with an axial ratio = 2.

include the dependency on the incidence angle θ (Fig. 6). The refraction indices n_H and n_V follow from the relation $\epsilon = n^2$. Dry snow is considered as a nonabsorbing medium, therefore, no imaginary parts appear in ϵ or n

$$n_H^2 = \epsilon_{\text{eff},H} = \epsilon_{\text{eff},x}$$

$$n_V^2 = \epsilon_{\text{eff},V} = \epsilon_{\text{eff},y} \cdot \cos^2 \theta + \epsilon_{\text{eff},z} \cdot \sin^2 \theta.$$

The CPD is then obtained from (2) with $\Delta n = n_H - n_V$, the volume thickness l and the wavelength λ of the system. Thus, the model, which was originally developed for L- and P-band [62], is easily transferable to other frequencies by using the appropriate value of λ and by adapting the dielectric constants in the case of dispersive materials. The model is independent of the absolute grain size and depends only on the axial ratio of ice grains. However, the size of the grains must be much smaller than the wavelength to avoid internal reflections in a spheroid, which might lead to additional phase differences [64]. According to the described model, Fig. 7 shows the CPD, which is expected to be measured by a radar sensor operating at a frequency of 9.65 GHz for various incidence angles. The expected CPDs have been calculated for the example of a 10-cm-thick snow slab. The CPD is a function of the axial ratio (horizontal-to-vertical) of oriented snow grains. Negative phase values are predicted for firn and metamorphic snow consisting of vertically aligned prolate grains, whereas positive phase values are predicted for fresh snow, which contains horizontally elongated oblate particles. For higher incidence angles, the phase difference increases due to two reasons. 1) The polarization vectors of the radar are better aligned with the optical axis of the bifractive medium. 2) For a fixed volume thickness, the propagation path of the waves through the volume itself increases with the incidence angle. Since $\epsilon_{\text{eff},i}$ depends also on the ice grains' volume fraction μ , the phase difference increases with snow density (see inset of

Fig. 7). According to the model, the CPD can be used to determine the thickness of an optically anisotropic medium like snow if the anisotropy is known. The anisotropy can be either estimated, modeled or measured. Measured CPD values of 5–15 deg/10 cm of fresh snow are presented in Sections IV-E and VI.

E. Multilayer Model

Typically, snow is not a homogeneous single layer. Different layers can consist of completely different crystal types. To account for different layers, the specific CPD must be calculated for every layer and the resulting phase differences must be added. Density and water content variations, refraction, absorption, and internal reflections between different layers must be considered as well. However, for low density variations and a cold, dry snow pack a mean specific CPD can be assumed to characterize the entire snow pack. When considering the difference in CPD between two nearby times, only changes of the snow pack are of interest. As snow fall and settling happens on faster time scales (hours) than snow metamorphosis (days to weeks), the change of the CPD can be used to determine the depth of a fresh fallen snow layer.

IV. TIME-SERIES DATA

A. Processing of Time-Series Data

The CPD as defined in (1) was extracted from the polarimetric coherence which is given as

$$\tilde{\gamma}_c = \gamma_c \cdot e^{i\phi_c} = \frac{\langle S_{VV} S_{HH}^* \rangle}{\sqrt{\langle |S_{VV}|^2 \rangle \cdot \langle |S_{HH}|^2 \rangle}} \quad (5)$$

S_{VV} and S_{HH} represent the single look complex (SLC) values. An ensemble average $\langle \cdot \rangle$ with a two-dimensional Gaussian weighting kernel with a full width of half maximum (FWHM) of 45×35 pixels was used, corresponding to an averaging window of 75×85 m.

B. Geocoding

The geocoding grid, which is contained in the TSX data set, is based on a coarse resolution digital elevation model (DEM) and shows a horizontal accuracy of ± 10 m. For a higher accuracy, the stripmap-SLC products were geocoded again by solving the range, Doppler- and ellipsoid equation including a local DEM with a resolution of 2 m and additional ground control points. The achieved geocoding accuracy was shown to be below 3 m by comparing the simulated interferograms based on the external DEM with interferograms calculated from TDM data. Geocoded scenes from different orbits matched on the pixel level with each other and confirmed the geocoding accuracy. Backscatter values, phase differences, and coherence values were calculated in radar coordinates and were transformed into WGS84 coordinates for comparison.

For time-series analysis, the 25-m resolution CLC map (Fig. 1) was used to determine average values for the backscatter signal, the CPD, and the magnitude of the copolar coherences for each

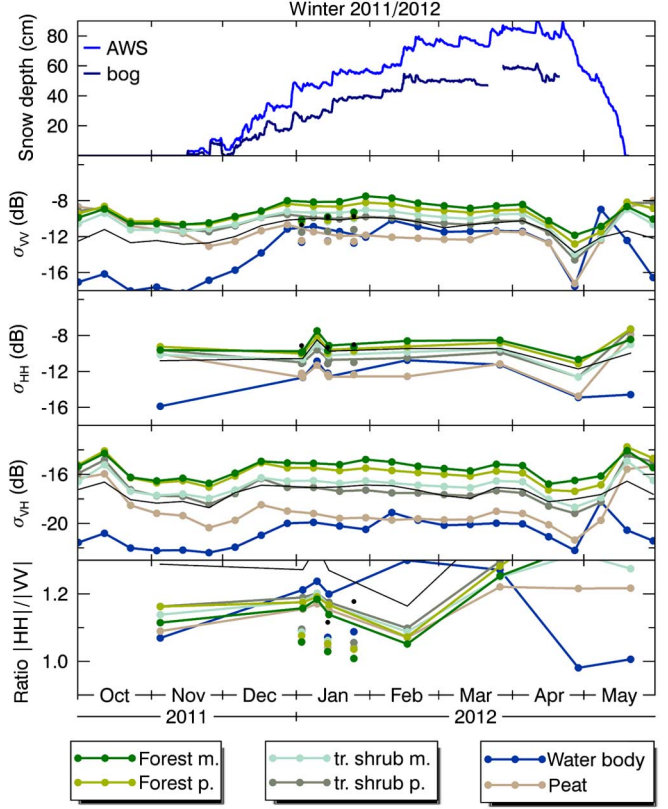


Fig. 8. Winter 2011/2012: time series of the backscatter signal σ_0 for typical land cover and soil types (m., mineral soil and p., peat) together with SD. Data of TSX (VV/VH) and TDM acquisitions (VV/HH) are shown together. In autumn, σ_0 drops by 2–4 dB for peat covered areas. During winter, σ_0 is 4 dB higher for forested areas than for peat-covered areas. Wet snow in autumn and spring reduces σ_0 by 2–5 dB. The thin black line indicates data of a singular point at the IOA covered by sparse trees.

land cover type. Averaging was used to avoid local effects of speckles or strong scatterers.

C. Discussion of Backscatter Signal σ_0

Radar backscatter signatures extracted from TSX (VV/VH) and TDM acquisitions (VV/HH) from the winter 2011/2012 are plotted in Fig. 8. A full time series of TSX acquisitions was available, whereas only a few acquisitions were available from TDM. For comparison, TDM data were plotted into the same graph in Fig. 8, which shows σ_{VV} . Both, TSX and TDM, show very similar backscatter values despite the slightly different incidence angles. The backscatter signal σ_0 in both polarizations, VV and HH, is typically 3–4 dB higher for forested regions and suggests the use of backscatter signal for forest/no-forest segmentation. The cross-pol backscatter signal (VH) of the peat area is very similar to the backscatter signal of the frozen water body and indicates a simple scattering mechanism like surface scattering. Too few acquisitions were available to make any assumption from the $|HH|/|VV|$ -ratio. For the next winter (2012/2013), two full time series of TSX acquisitions were available, one in VV and HH polarization and the other in VV and VH polarization. Both had almost the same incidence angles (32.7° and 33.8°) and show a very similar backscatter signal σ_{VV} as shown in Fig. 9.

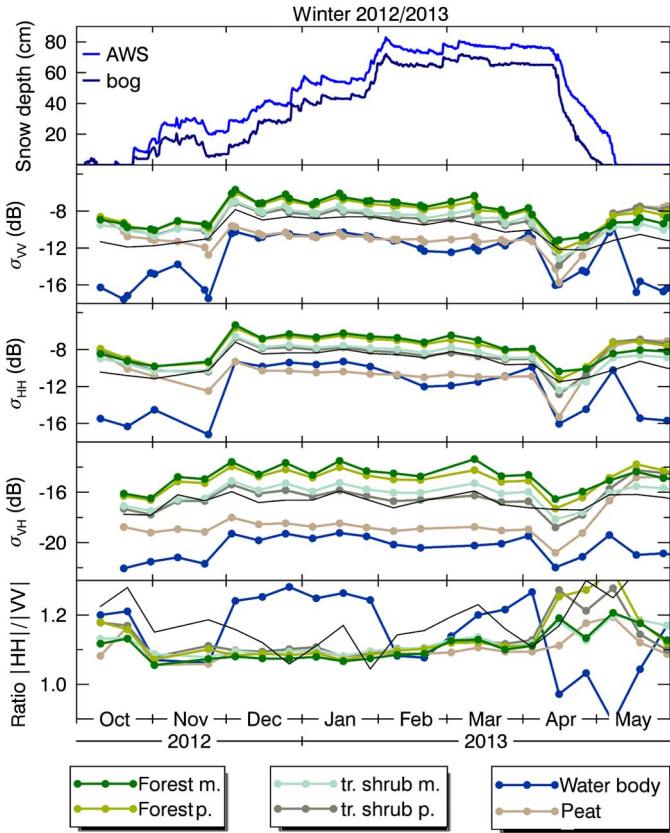


Fig. 9. Winter 2012/2013: time series of the backscatter signal σ_0 for typical land cover and soil types (m., mineral soil and p., peat) together with SD. Data of TSX (VV, HH, and VH) and TDM acquisitions (VV/HH) are shown together. In winter, σ_0 reduces by 2–4 dB for peat-covered areas compared to autumn and spring. Forested areas show a 4 dB higher σ_0 than peat-covered areas during winter. Wet snow in autumn and spring reduces σ_0 by 2–5 dB. The thin black line indicates data of a singular point at the IOA covered by sparse trees.

Concerning snow accumulation, no significant trend was found in both time series. In contrast, snow melt is visible at the end of April 2012 and mid of April 2013 by a strong decrease in the backscatter signal of 3–4 dB for forest and shrub and 5–6 dB for bog and the lake (water body). The freezing of the lake during December 2012 and early December 2013 is also observable by an increase in backscatter signal of 4–6 dB of the typically very low signal of open water. The lake remains frozen during snow melt and melts 3–4 weeks later.

D. Copolar Phase Difference

Compared to the backscatter signal, the CPD increased significantly between November 2011 and January 2012 as shown in the time series given in Fig. 10. The CPD depends on land cover type. Higher effects are observed for shrub ($+18^\circ$) and peat ($+22^\circ$) compared to forested area ($+13^\circ$). Although the CPDs in February and March are still higher than in autumn or spring, they cannot be linked directly to SD. However, up to 20 cm of snow fell 3 days before the acquisitions in January with additional snow fall of 30 cm up to 4 weeks before. During the whole December temperatures were between 0 and -10°C such that it is presumed that only weak and slow temperature gradient driven recrystallization occurred. Consequently, the horizontal structure of fresh snow has been preserved, such that positive

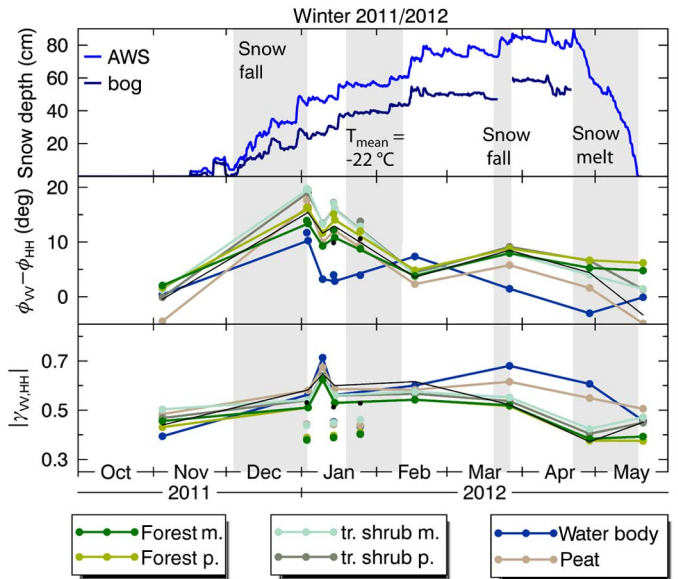


Fig. 10. Winter 2011/2012: time series of the CPD and magnitude of the copolar coherence. Relevant meteorological events are shaded. The CPD increases during snowfall and returns to autumn values in spring. The copolar coherence is higher during winter. The low coherent values at three dates in January are from acquisitions with an incidence angle of 41.2° , which had a poorer data quality and resolution. Still, they showed almost the same phase differences as the other acquisitions (see also Fig. 19). The thin black line indicates data of a singular point at the IOA covered by sparse trees.

phase differences were measured in January. The cold temperatures between January and February (Fig. 3) lead to a strong recrystallization, such that the phase differences disappeared until the mid of February. The small increase of the CPD ($+5^\circ$) at the end of March can be linked to 15 cm of snowfall 4 days before the acquisition. After snow melt in April, peat covered areas show negative phase differences (-5°) similar to the snow free acquisition in October.

To verify the assumption that fresh snow causes positive phase differences, a complete time series of 21 dual-pol (VV/HH) TSX scenes was acquired during the winter 2012/2013 with a temporal resolution of 11 days. The CPD in Fig. 11 shows a significant increase of 4–8 deg/10 cm of fresh snow after each of the major three snowfall events. Shrub and peat areas show up to twice as high changes in the CPD as observed for forested areas. The phase values decrease by time when no fresh snow is falling. In March 2013, temperatures stayed well below zero ($T_{\text{mean}} = -13^\circ\text{C}$) and no precipitation occurred for more than 4 weeks (Fig. 4). Within the same time, the CPD reached maximal negative values (Fig. 11).

Assuming that freezing soil would cause this negative change of CPD, this would be contradictory to the observation in the year before, where the highest positive phase differences were observed early January during soil freezing. In the year after, soil freezing happened at the end of November (see Fig. 4). At the same time, the CPD stays constantly low at $0^\circ \pm 2^\circ$ while the copolar coherence $|\gamma_{VV,HH}|$ increased significantly. Eleven days later, during the second snow fall from 4 to 15 December, when the soil was already frozen, the CPD changed by 5° – 7° together with 10–15 cm of fresh snow. For snow free conditions, in October and May, only peat covered areas show negative phase differences, whereas all other land cover types show a CPD of $0^\circ \pm 2^\circ$.

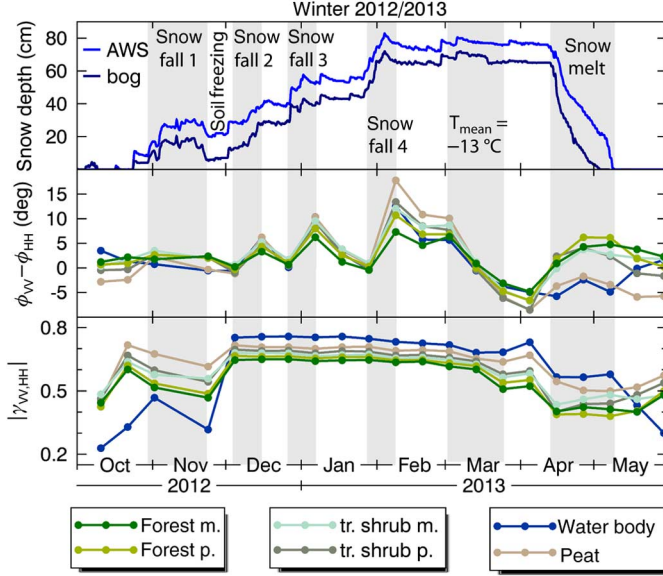


Fig. 11. Winter 2012/2013: time series of the CPD and magnitude of the copolar coherence $|\gamma_{VV,HH}|$. Relevant meteorological events are shaded. The CPD increases significantly by 4–8 deg/10 cm of fresh snow for each of the three major snowfall events (#2–#4). After soil freezing $|\gamma_{VV,HH}|$ stayed constantly high while negative air temperatures persisted.

E. Temporal Correlation with Snow Fall

For a more quantitative analysis how fresh snow affects the CPD, the change of CPD is shown as a function of the amount of fresh snow within 11 days for different land cover types in Fig. 12(a)–(c). As snow requires a few days for settling, only snow which had been fallen between $t - 11$ days and one day before the acquisition ($t - 1$ day) was considered for comparison with the change of the CPD between $t - 11$ days and t . The CPD correlates well with the depth of fresh snow ($R^2 > 0.8$) and shows highest values for peat and higher values for frozen water and shrub than for forested areas. Root-mean-square errors (RMSEs) are below 3° and 3 cm. Numerical values are shown in Table III. For forested areas, the tree canopy partially covers the ground, such that the signal is disturbed and the CPD is lower. Areas covered by transitional shrub contain also some sparse trees and vegetation. Note, that the CPD values measured for the ice covered water body are very similar to the values of open peat and tr. shrub on peat.

Fig. 12(d) shows that the CPD decreases by 3–9 deg/11 days for mean temperatures between -12 and -18°C as long as no snow fall occurs. The temporal change of the CPD shows a large spread of values for warmer temperatures, depending on whether snow fall occurred or not. This agrees with the observation that positive phase differences are not caused by soil freezing but originate from fresh snow.

V. PROCESSING OF SNOW TRANSECT DATA

Spatial correlations were calculated from snow transect measurements of the winter 2011/2012, to supplement the temporal correlations of Section IV-E. The processing was done as follows: 1) selection of ground measurements corresponding to the date of the SAR acquisitions; 2) calculation of CPD;

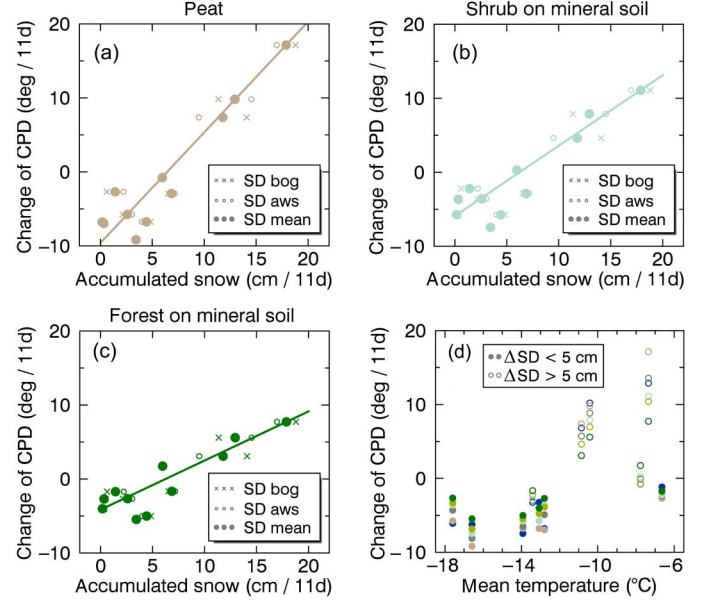


Fig. 12. (a)–(c) Change of CPD as a function of accumulated snow within intervals of 11 days (winter 2012/2013). Only acquisitions are considered, which were taken during temperatures well below zero (December 1, 2012 to April 11, 2013). SD values vary by up to 3 cm between the bog site and the AWS and have been averaged (SD mean) to calculate the regression (line). Numerical results are given in Table III. (d) Change of CPD over the mean temperature of each 11 day interval. Symbols distinguish periods with more (open symbols) and with less than 5 cm of snow accumulation (ΔSD) (filled symbols). The color indicates different land cover types according to Fig. 1.

TABLE III
RESULTS FROM LINEAR REGRESSIONS: CHANGE IN CPD ($\Delta\phi_c$) VERSUS ACCUMULATED SNOW WITHIN 11 DAYS (ΔSD) AS SHOWN IN FIG. 12(A)–(C) GIVEN IN DEGREE PER DECIMETER (DEG/dm). RMSEs AND R^2 -VALUES ARE ALSO GIVEN

Land cover type	$\Delta\phi_c = m \cdot \Delta\text{SD} + c$	RMSE			
	slope m (deg/dm)	offset c (deg)	R^2	$\Delta\phi_c$ (deg)	ΔSD (cm)
Forest on mineral soil	6.6	-4.1	0.78	1.9	2.9
Forest on peat	8.7	-5.2	0.83	2.2	2.5
tr. shrub on mineral	9.5	-5.9	0.83	2.4	2.5
tr. shrub on peat	11.7	-7.3	0.85	2.6	2.2
Frozen water body	11.2	-7.1	0.81	2.9	2.6
Peat	15.0	-9.6	0.88	2.8	1.8

3) selection of valid pixels and classification for forest/no-forest separation; 4) geocoding and adapting the spatial resolution of the ground measurements to the radar resolution; and 5) calculation of correlation curves. The following sections describe the five steps in detail. Section V-F discusses the effect of the smoothing window size.

A. Selection of Scenes and Ground Measurements

Ground campaigns were not conducted exactly at the same time as satellite-observations, therefore, a careful selection was done. As SD and structure changes with time, ground measurements were excluded, which lie too long before or after the acquisition and which are “separated” by snow fall or melting events from the time of acquisition. Table IV shows which field campaigns were used for each TDM-acquisition.

TABLE IV
DATES OF GROUND CAMPAIGNS WHOSE SD TRANSECT DATA WERE USED FOR ANALYSIS TOGETHER WITH A TDM-SCENE OF A SPECIFIC DATE

Date of TDM scene	Closest matching campaign dates
2011-11-04	- no snow -
2012-01-03	2012-01-09, 2012-01-10
2012-01-09	2012-01-09, 2012-01-10
2012-01-14	2012-01-09, 2012-01-10
2012-01-25	2012-01-23, 2012-01-24
2012-02-16	2012-02-22, 2012-02-23, 2012-02-24 2012-02-25, 2012-02-26
2012-03-26	2012-03-23
2012-04-28	- no snow -
2012-05-20	- no snow -

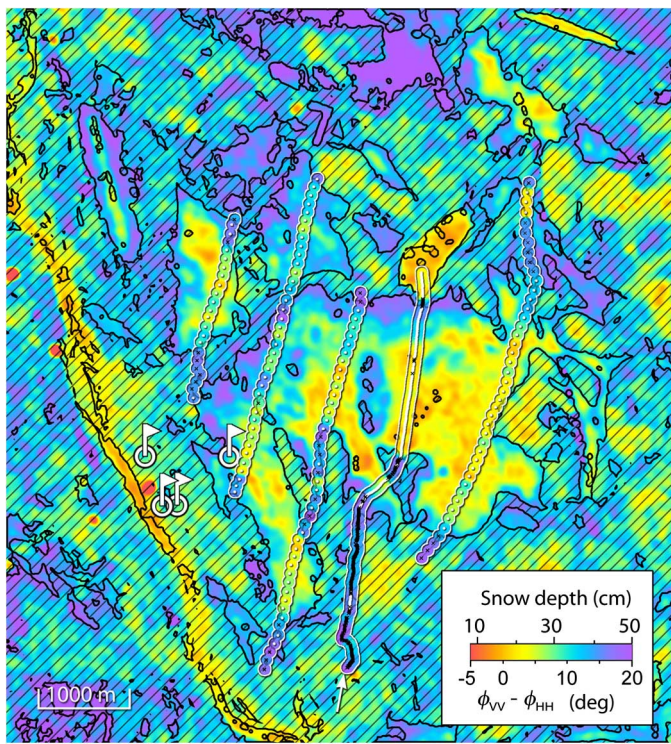


Fig. 13. Colored-coded CPD from January 9, 2012. Five SD transects from campaigns of January 9 and 10 are plotted as dots with white outlines. The dots indicate the exact location of SD measurements. Excluded SD measurements are marked by black dots. The white outlines are filled with the averaged SD measurements, which were color-coded by the upper color bar. Hashed areas mask out forested areas. A cross section along the transect with the white arrow is shown in Fig. 15.

B. Calculation of CPD

The CPD was calculated according to Eq. (5). A smoothing window of 54×39 pixels was used, corresponding to an averaging window of 91×91 m, 115×91 m, and 74×121 m depending on incidence angle ($\theta = 32.7^\circ$, 39.7° , and 41.5°). As each TDM dataset contains one TDX and one TSX acquisition, the coherence $\tilde{\gamma}_c$ was calculated separately and both were averaged: $\tilde{\gamma}_c = \frac{1}{2}(\tilde{\gamma}_{c,tsx} + \tilde{\gamma}_{c,ttx})$ (this step is optionally, but enhances the SNR by a factor of $\sqrt{2}$). A color-coded image with the extracted phase values is shown in Fig. 13.

The availability of two acquisition at exactly the same time made it possible, to get a figure about the accuracy of the phase

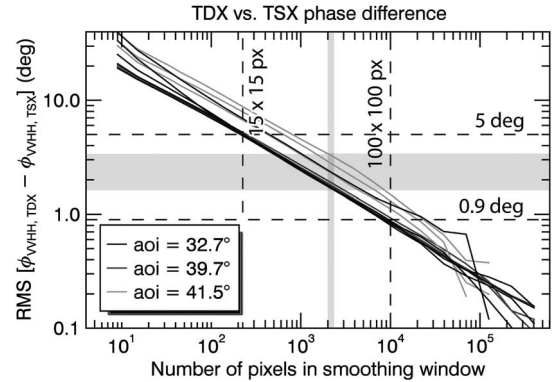


Fig. 14. RMS difference between the CPDs of the two dual-pol acquisitions contained in one TDM scene. Different lines show the rms-phase noise for different acquisitions. The used smoothing window of 54×39 px allows a phase measurement with an accuracy of $\pm 3^\circ$ (shaded).

measurements, because the two acquisitions from the satellites TSX and TDX are independent measurements. The root mean square (rms) difference between the CPD values from the TSX and the TDX acquisition are shown in Fig. 14 for different smoothing window sizes. The rms accuracy for the CPD is better than $\pm 3^\circ$ for a window of 54×39 px as used in this study. While noise decreases with more smoothing, resolution is lost. Section V-F describes how the optimal smoothing window was found.

C. Selection of Valid Pixels

In forested areas, the relationship between CPD and SD is disturbed by the vegetation cover. Therefore, forested areas were excluded from the analysis. A simple forest/nonforest classification based on thresholding the backscatter intensity was performed. The threshold was set to the median of the backscatter signal σ_0 in dB of the scene. To consider the speckle effects, a Gaussian smoothing window of 21×16 pixels was applied before calculating the median. The scene-specific threshold, which splits the scene into 50% forest and 50% unvegetated areas, was verified by the CLC map (Fig. 1). The backscatter image from January [Fig. 2(b)] and the time series shown in Fig. 8 show a difference in backscatter signal of about 4 dB between forest and other land cover type during winter. Pixels where the absolute value of the polarimetric coherence was lower than 0.5 were not analyzed. Therefore, areas where the signal is below the noise level and where targets contain significant volume scattering were excluded. The masked areas are shown in Fig. 13 by the black single hatched areas confined by black outlines.

D. Preprocessing of Ground Measurements

SD datasets were available with thousands of samples due to a few kilometers long transects (Table II). SD was measured every 10–100 m with a hand-held GPS with an accuracy of a few meters. The coordinates were converted into radar coordinates to compare SD with the corresponding CPDs. The location of SD samples are shown in Fig. 13 as white (used) and black (excluded) dots. The snow samples of a transect with 561 points appear as a black and white line (arrow). A cross section along this

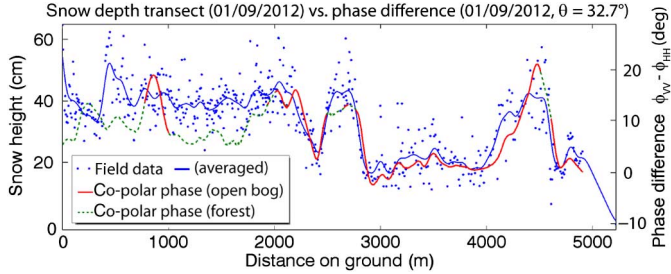


Fig. 15. Measured SD (dots) and CPD (red line) along a 5-km long transect. The solid blue line represents the averaged ground measurements. Masked forested sections are shown as green dashed lines.

transect is shown in Fig. 15. The solid blue line shows the point samples, which were smoothed along the transect with the same smoothing window as it was used to calculate the copolar coherence. Adapting the spatial resolution is necessary to average out SD variations below the resolution of the CPD of around 50–100 m.

The spatial resolution was adapted as follows: in cases where the spacing between point-like ground measurements was smaller than the spatial resolution of the smoothed copolar phase, the ground measurements were averaged using a discrete-kernel approach. Namely, each coordinate of an SD measurement was convolved with a 2-D-Gaussian smoothing kernel, where the wings were clipped at 60% of maximum. When the clipping radii of neighboring pixels were overlapping, then the SD values were calculated as a weighted average. Because almost all SD measurements have a spacing of 100 m or less, nearly all neighboring points were averaged. The white outlines of the transects in Fig. 13 are filled with the averaged SD data by using the same color table as for the CPD, but scaled by the regression results from January 9, 2012 as shown in Section IV.

E. Comparison With Ground Measurements

CPD values, which were located within the proximity of a ground measurement, were analyzed. The proximity (limited by white outlines of the transects in Fig. 13) is defined by the clipping edge of the discrete-kernel approximation, resulting in an elliptical area of 65×47 pixels around the exact coordinate of the ground measurement. Pixels, which are too close together, are statistically not independent due to the smoothing process. To avoid correlated pixels and to achieve a homogeneous sampling, points were selected, which are as close as possible to the location of a ground measurement, but which do not have neighboring points within a distance of half the smoothing window size. This was achieved by modeling repulsive particles (sample points where the phase values were extracted) on an attractive potential (location of ground measurements) and minimizing the total energy. The extracted CPD values were plotted against the preprocessed ground data as 2-D-histograms, equivalent to a scatter plot, which include the point density. A regression line was fitted to the scatter plot. For results, see Section VI.

F. Optimal Size of Smoothing Window

Correlation parameters were evaluated for different sizes of smoothing windows. The goodness-of-fit parameter R^2 has a

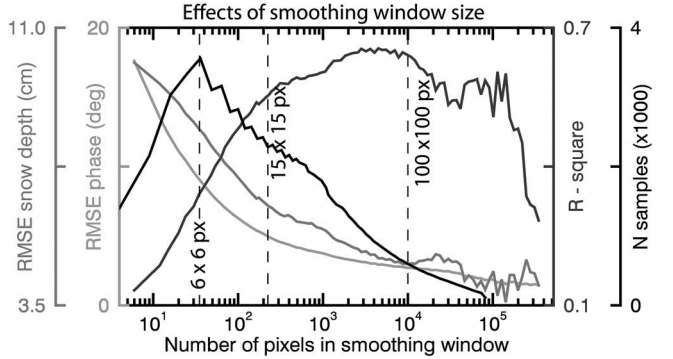


Fig. 16. Effect of the size of the smoothing window on the statistics of the scatter plot in Fig. 17(c). Window sizes between 15×15 and 100×100 px show the best R^2 values. For details see Section V-F.

maximum for window sizes between 15×15 and 100×100 px as shown in Fig. 16. For window sizes below 15×15 px, the fluctuations of the phase dominate and degrade the correlation. Because the ground data were averaged on the same scale as the radar acquisitions, smoothing windows above 100×100 px will not only average out smaller variations of the CPD but also variations of SD measurements. Consequently, the spread of CPD and SD values will decrease, such that the correlation, measured by R^2 , decreases. Fig. 16 shows the RMSE of the measured CPD versus the estimated CPD from linear regression. For a smoothing window of 54×39 px, the RMSE for ϕ_c shows an accuracy of $\pm 4^\circ$, which is only 1° above the phase-noise of the system as shown in Fig. 14, 19, and Table VII. The RMSE of the inverse, the estimated SD versus the measured SD, show an accuracy of ± 5 cm. The number N of samples used for regression initially increases with window size (Fig. 16, black line). The reason is that more space for independent samples is available on the disks, which are determined by the smoothing kernel around the ground measurements and which begin to form a connected surface. For window sizes larger than 6×6 px, the number of samples decreases, because not every ground measurement can be used, as neighboring samples were averaged. Around 1000 samples were used for each scatter plot in Figs. 17 and 20.

VI. ANALYSIS OF SNOW TRANSECT DATA

A. Correlations With Snow Transects

Section IV-E showed a correlation between the temporal variation of accumulated fresh snow and the CPD. In this paragraph, spatial variations of early season snow and the CPD are used to derive very similar correlations. The large number of distributed SD measurements of the winter 2011/2012 were analyzed. Fig. 17(a)–(c) shows scatter plots between SD and CPD for January 9 and 14, 2012 for three different incidence angles. The three dates were chosen, as despite the temporal difference of 5 days, the meteorological and snow conditions were very similar. The three plots have the same ground data on the x-axis but differ in slope and y-axis intercept. Table V summarizes regression results for the three datasets. Based on the model of Section III, the CPD was calculated for $\lambda = 3.1$ cm

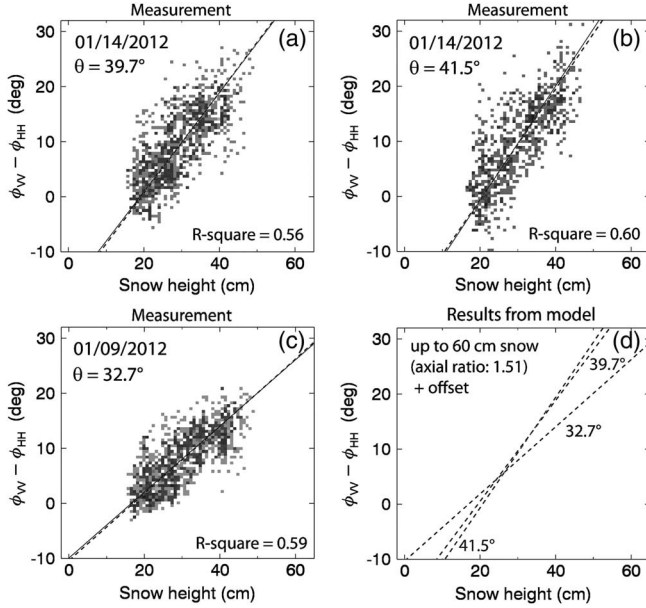


Fig. 17. CPD as a function of SD for different incidence angles. Regression (solid lines) are plotted together with results based on the theoretical model (dashed lines) presented in Section III. Reasons for the y-axis intercept are described in Section VI-B.

TABLE V
REGRESSION PARAMETERS COMPARED WITH MODELED RESULTS FOR THE CPD
(axial - ratio = 1.51 AND FREE OFFSET) AS SHOWN IN FIG. 17

Acquisition		Linear regression			Model	
Date (mm-dd)	aoi (θ)	Slope (deg/dm)	Offset (deg)	R^2	Slope (deg/dm)	Offset (deg)
01-09	32.7°	6.0 (1)	-10.0 (3)	0.58	6.1	-10.0
01-14	39.7°	8.9 (2)	-17.2 (4)	0.56	9.1	-17.6
01-14	41.5°	10.4 (2)	-21.5 (5)	0.60	10.0	-20.5

The $1 - \sigma$ uncertainty in brackets refers to the last given decimal place. The slope is given in degree/decimeter (deg/dm).

and the incidence angles of the three acquisitions. The snow density of 0.2 g/cm^3 was based on snow pit measurements during the campaigns. A axial ratio of the ice grains of 1.51 was used for all three acquisitions. The offset of the y-axis intercept was freely chosen as the model does not include properties of an underlying ground. The results from the model are shown in Fig. 17(d) and Table V and were also drawn into the graphs in Fig. 17(a)–(c) for a better visual comparison. The negative y-axis intercept could also be modeled by a layer of depth hoar with vertically elongated snow grains. Snow pits at the IOA site and the bog site confirm a 3–7-cm-thick layer of depth hoar. Including a second snow layer with a constant thickness of 10 cm and vertically elongated grains with a axial ratio of 0.43 would yield to offset values of -17.5° , -22° , and -11.5° for the incidence angles $\theta = 39.7^\circ$, 41.5° , and 32.7° , which corresponds by $\pm 1.5^\circ$ to the measured offsets given in Table V.

B. Snow Free Reference Phase

The observed negative offset is not necessarily a pure contribution of depth hoar. In May, after all snow has melted, the CPD of the bog area returns to $-5^\circ \pm 2^\circ$, which was also observed during November in the time series of Figs. 10 and 11.

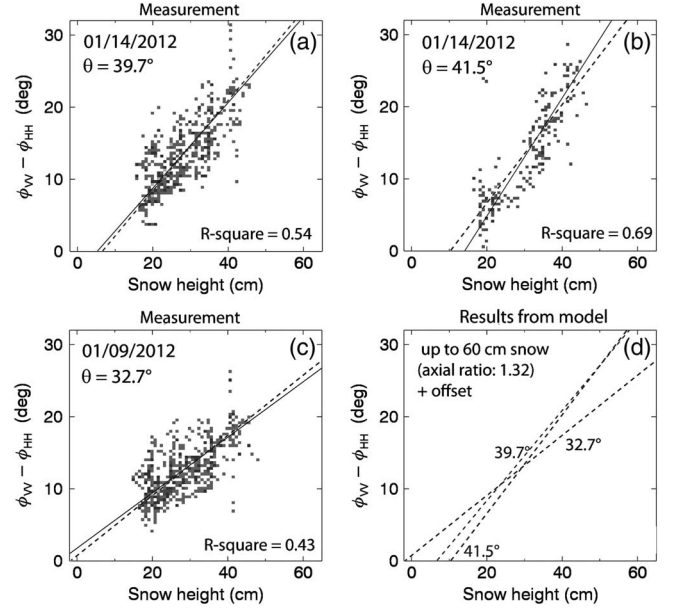


Fig. 18. CPD relative to snow free acquisitions as a function of snow height. The negative offset is much smaller compared to Fig. 17. Note that a different scaling for the y-axis is used here.

TABLE VI
REGRESSION PARAMETERS COMPARED WITH MODELED RESULTS FOR THE CPD
(axial - ratio = 1.32; FREE OFFSET)

Acquisition		Linear regression			Model	
Date (mm-dd)	aoi (θ)	Slope (deg/dm)	Offset (deg)	R^2	Slope (deg/dm)	Offset (deg)
01-09	32.7°	3.9 (3)	+1.6 (5)	0.43	4.2	+0.7
01-14	39.7°	5.9 (3)	-3.1 (6)	0.54	6.3	-4.3
01-14	41.5°	8.2 (4)	-11.7 (10)	0.69	6.8	-7.1

The CPD of snow-free dates was subtracted and considered as background (Fig. 18). The $1 - \sigma$ uncertainty in brackets refers to the last given decimal place. The slope is given in degree per decimeter (deg/dm).

Consequently, a background (reference) phase is likely and could explain the observed negative offset. To investigate the effect of a background phase, snow-free acquisitions were used as a reference $\phi_{c,\text{ref}}$. Phase differences $\phi_{c,\text{rel}}$ relative to the background were analyzed

$$\phi_{c,\text{rel}} = \phi_c - \phi_{c,\text{ref}} \quad (6)$$

with $\phi_{c,\text{ref}} = \frac{1}{2}(\phi_{c,\text{Nov.}} + \phi_{c,\text{May}})$. Due to the reference phase, the noise-figure increases, as both phases contribute independently to the phase error and lead, according to error propagation laws, to an uncertainty of $\delta\phi_{c,\text{rel}} = \sqrt{(\delta\phi_c)^2 + (\phi_{c,\text{ref}})^2} = 4 - 5^\circ$. Also, less data points with a sufficiently high coherence were available as only points with $|\gamma_{VVHH}| \geq 0.45$ in both, the snow-free reference and the scene of interest, were selected. The obtained correlations are plotted in Fig. 18 and are summarized in Table VI. The negative offsets are much closer to zero compared to Table V. The slopes of the correlation plots would result in an axial ratio of 1.32 for the ice grains. The difference of 10%–15% in the size ratio compared to Fig. 17 can be attributed to the higher noise and the uncertainty of the fit.

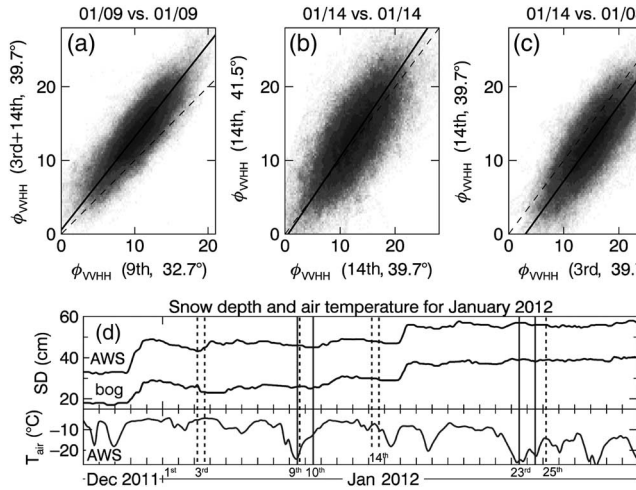


Fig. 19. (a)–(c): CPD of different acquisitions plotted against each other as 2-D-histograms (CPD in degree). Solid line: regression, dashed-line: unity slope. The graphs verify the angle dependence of the model and check the consistency of CPD between different incidence angles (a) and (b) and times (c). For (a), two acquisitions (January 3 and 14) were averaged as the acquisition of the 9th was taken almost exactly in between. (d) About 3 cm of fresh snow fell between the acquisitions from 3rd, 9th, and 14th. Temperatures varied around $-8 \pm 3^\circ\text{C}$ with two colder days around the ninth. Vertical solid lines: dates when snow transects were measured, dashed lines: dates of acquisitions.

C. Dependence on Incidence Angle

The availability of five acquisitions within 11 days from different orbits made it possible to analyze the dependence on incidence angles. All CPD values of forest-free areas from each two acquisitions with different incidence angles were plotted against each other. Two examples are shown as 2-D-histograms in Fig. 19(a) and (b). Table VII (line 1–4) summarize the results. For January 3 and 14, 2012 two acquisitions were available with only 13 h time difference. To compare with the acquisition from the 9th ($\theta = 32.7^\circ$), the mean value of two acquisitions from the 3rd and 14th was used. Higher CPDs were measured for larger incidence angles. Compared with the measured CPD-ratios, the model overestimates the angle-dependence by 25%.

The inter-orbit comparison provides also a figure about the inter-orbit phase noise: Line 1–4 of Table VII show, that the rms-difference of the CPD between acquisitions is below 3.7° . This is in good agreement with Fig. 14, which shows that the rms phase noise between the two satellites TSX and TDX is less than 3° . The acquisitions with an incidence angle of 41.5° show around 1° more rms phase-noise than the other acquisitions, which was already observed in Fig. 14. The higher phase noise also explains the lower coherence values of the “outliers” of $|\gamma_{VVHH}|$ in January as shown in Fig. 10.

D. Temporal Evolution of Phase Differences

The CPD as shown in the time series in Fig. 10 drops significantly at the end of January. Fig. 20 shows the correlation between CPD and SD for the associated dates. Table VIII contains the correlation parameters. After an initial increase in January, the slope of the correlation decreases by time. The values of the y-axis intercept drop from -5° to -23° from early- to late January. The correlation is very weak at the mid of February and March and disappears at the end of April when all phase values are within $0 \pm 3^\circ$.

TABLE VII
REGRESSION PARAMETERS FROM INTER-ORBIT CPD-COMPARISON (FIG. 19), EXPECTED CPD-RATIOS BETWEEN DIFFERENT INCIDENCE ANGLES FROM THE MODEL AND INTER-ORBIT RMS NOISE

Acquisition (y-vs.-x) day of Jan., θ , (subfig from 19)	Regression CPD- ratio	Model CPD- ratio	RMS- diff. (deg)	
03rd (41.5°) vs. 03rd(39.7°)	1.06(3)	-1.3(5)	1.09	3.7
09* (39.7°) vs. 09th(32.7°), (a)	1.26(2)	+0.6(2)	1.49	2.5
09* (41.5°) vs. 09th(32.7°),	1.30(3)	+0.3(3)	1.63	3.4
14th (41.5°) vs. 14th(39.7°), (b)	1.10(3)	-0.7(3)	1.09	3.7
14th (39.7°) vs. 03rd(39.7°), (c)	1.02(3)	-2.9(4)	1.00	3.0
14th (41.5°) vs. 03th(41.5°)	1.07(4)	-2.9(7)	1.00	4.1

* denotes the mean value of the two acquisitions from January 3 and 14.

Between January 3 and 14, settling of the snow layer causes some densification [Fig. 19(d)]. In consequence, a stronger dependence on the particle shape is expected. The density of snow increased by 5%–10%, which is confirmed by snow pit measurements. The specific CPD (given in deg/10 cm) depends quite linear on snow density for densities around 0.2 g/cm^3 such that the CPD is also expected to increase by 5%–10% (inset, Fig. 7). Table VIII shows that the specific CPD increases from 8.1 to 8.9 deg/dm (+10%) for $\theta = 39.7^\circ$ and from 7.2 to 10.4 deg/dm (+44%) for $\theta = 41.2^\circ$. The direct comparison of CPD values for the same incidence angle but with 11 days time difference (Fig. 19(c), Table VII, l. 5+6) in January 2012 shows indeed a slight increase in the CPD-ratio (+2%, +7%). A global decrease by 2.9° could be an effect of weak temperature gradient driven metamorphism or depth hoar growth.

According to Fig. 3, there were no major snowfalls between the acquisitions from January 25, and February 16. The mean air temperature dropped to -22°C between January 25 and February 16. The soil temperature stayed just below the freezing point due to the isolating effect of 40 cm of snow in the bog area. Thus, the resulting temperature gradient dropped from 30 K/m in January to 55 K/m and reached its maximum, when the air temperatures dropped below -30°C early February with values up to 80 K/m . According to the thermodynamics of snow, the strong temperature gradient in early February caused a fast recrystallization due to vertical water vapor transport between the snow crystals [9]. The snow crystals reorganize from horizontally elongated oblate particles to more spherical or even vertically elongated particles [9]. The timescale for a complete recrystallization cycle of snow grains is on the order of a few days for gradient values of 50 K/m [2], which implies that the horizontally oriented oblate particles will disappear within a few days. This would explain the fast decay of the observed phase difference within 1–3 weeks as shown in Figs. 10 and 20 for the three acquisitions from January 14, January 25, and February 16. Keeping the metamorphosis of snow in mind and applying the model described in Section III, the CPD would turn from positive to zero or even to negative values (see Fig. 7). The time series from 2012/2013 shows the same effect during March 2013 (Fig. 11).

Due to the mild temperatures close below zero in December 2011 and early January 2012, the fresh fallen snow might have been prevented from fast recrystallization such that positive phase differences were preserved and the SD could be determined by means of CPD, which is normally only sensitive to the

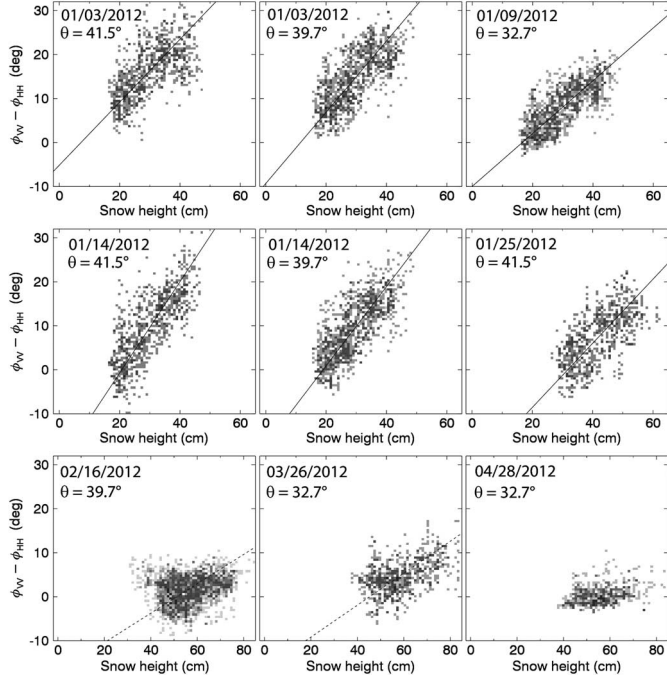


Fig. 20. Correlation between snow height and CPD for all available acquisitions from winter 2011/2012. The snow in the last graph (April) is wet and shows less phase fluctuations than the other plots as only scattering at the snow surface occurs.

TABLE VIII
REGRESSION PARAMETERS OF CPD VERSUS SD FROM SNOW TRANSECTS OF DIFFERENT CAMPAIGNS

Acquisition	aoi (θ)	Slope (deg/dm)	y-axis (deg)	R^2	Mean $\langle \phi_c \rangle$ (deg)
2012-01-03	41.5°	7.2 (3)	-5.2 (6)	0.41	
2012-01-03	39.7°	8.1 (2)	-9.3 (5)	0.52	
2012-01-09	32.7°	6.0 (1)	-10.0 (3)	0.58	
2012-01-14	41.5°	10.4 (2)	-21.5 (5)	0.60	
2012-01-14	39.7°	8.9 (2)	-17.2 (4)	0.56	
2012-01-25	41.5°	7.3 (2)	-23.1 (7)	0.43	
2012-02-16	39.7°	[2.4]	[-15.4]	[0.06]	2 (2)
2012-03-26	32.7°	[3.4]	[-12.4]	[0.22]	4 (2)
2012-04-28	32.7°	[-]	[0.1]	0 (1)	

The $1 - \sigma$ uncertainty (in brackets) refers to the last given decimal place. Square brackets exclude values where the regression failed ($R^2 < 0.3$). The slope is given in degree per decimeter (deg/dm).

depth of fresh snow. During melt season, when the snow becomes wet and microwaves are reflected at the surface, the CPD reaches values close to zero. The last graph in Fig. 20 shows much less phase noise than all other graphs as mainly scattering at the wet snow surface occurs. Referring to the observed CPD in the paper of [44], the phase difference of $+150^\circ$ decayed within hours when the air temperature rose up to $+12^\circ\text{C}$ during daytime such that melting was triggered immediately. Interestingly, the CPD increased again during the evening and the next night up to 30° – 40° with negative night temperatures and dropped close to zero after sunrise ($+6^\circ\text{C}$).

E. Contribution of Soil Moisture to the Copolar Phase

Not only snow causes a CPD but also soil moisture causes a small CPD. Positive phase differences $\phi'_c = \phi_{\text{HH}} - \phi_{\text{VV}}$ were

modeled and measured in the range 0° and $+30^\circ$ for incidence angles 30° to 45° for unvegetated but rough soil at various frequencies [65]–[67]. A very high standard deviation of more than 20° is also common due to the rough soil. Positive phase differences were also observed [68], with lower values for C-band ($+11^\circ$) than for L-band ($+24^\circ$). Note that throughout this paper, the opposite sign convention was used ($\phi_c = \phi_{\text{VV}} - \phi_{\text{HH}}$), which would result in negative phase differences for the mentioned publications. This agrees with the negative values of $\phi_c = -5 \pm 2^\circ$, which were measured for the snow free acquisitions. The observed positive CPDs are, therefore, attributed to the anisotropic structure of fresh snow.

VII. SUMMARY

The CPDs $\phi_c = \phi_{\text{VV}} - \phi_{\text{HH}}$ of X-band SAR acquisitions from TerraSAR-X and TanDEM-X were analyzed and compared with SD measurements. The spatial information of a few kilometers long SD transect from the winter 2011/2012 was used to show a spatial correlation between the depth of fresh snow and the CPD. Nine TanDEM-X acquisitions with three different incidence angles were analyzed. For the winter 2012/2013, a complete time series of 21 TerraSAR-X acquisitions was used together with two time series of fixed weather stations to show a temporal correlation between fresh snow and the change of CPD for different land cover types.

The spatial correlations show a dependency of 6 – 10 deg/10 cm of snow, which accumulated within 4 weeks before the acquisitions. The temporal correlations show a dependency of 10 – 15 deg/10 cm for snow, which fell up to 11 days before the acquisition. The CPD of areas with sparse or no vegetation shows a stronger dependence on fresh snow than forested areas, where the snow is partially covered by the tree canopy. In both years, the CPD decreased by 3 – 7 deg/11 days when no snow fall occurred and temperatures were well below zero. A faster decrease was observed for stronger temperature gradients within the snow pack. A phase noise analysis was done by comparing acquisitions from the two satellites and from different orbits at similar times and various incidence angles. Between different acquisitions, a consistency of 3.5° rms for the CPD at a resolution of 54×39 pixels was found, corresponding to a spatial resolution of 91×91 m.

In this paper, positive CPDs were linked to the depth of fresh fallen snow. Slowly decreasing CPDs are interpreted with respect to the metamorphosis of the microstructure of snow. An analysis by the Swiss Institute for Snow and Avalanche Research (SLF) monitored the temporal recrystallization process of the ice grains in a snow sample under a vertical temperature gradient of 50 K/m [2]. They showed that the ice grains change their shape within a few days to weeks from horizontally extended oblate to vertically aligned prolate particles. The recrystallization speed depends mainly on the temperature gradient and can happen within a few days for strong temperature gradients.

To link the observed CPD with the microstructure of snow, a model is presented, which derives a birefringent refractive index from the anisotropy of ice grains. Based on the birefringence, the model is able to explain the observed CPD. The model, which was originally developed to explain a negative phase differences in firn and ice [62] could be extended to fresh

snow, because information about the horizontal structure of fresh snow has been published [1], [2]. The model does not include a background signal from soil, which was considered as an additional negative offset phase. The model was tested for different incidence angles and seems to overestimates the dependence on incidence angle by 25%. As input parameter, the anisotropy of snow is required, whose determination is a current topic of research. Apart from sophisticated optical [44] or computer tomography analysis [1], snow pack models [69], the thermal conductivity [45] and the CPD itself could help to determine the anisotropy of snow.

The dependence of the CPD on fresh snow opens new possibilities to detect quantitatively snow fall, which is up to now poorly or not at all covered by any of the optical, passive or active microwave remote sensing sensors. There is a strong need for spatially detailed snow observations for climate modeling, weather forecasts, water storage, and hydrology [70]–[73]. In this paper, the presented correlations show an RMSE of ± 6 cm for SD for spatial correlation without any reference and an RMSE of ± 3 cm when changes in the CPD within 11 days are considered. The phase noise of the TanDEM-X sensor of $\pm 3.5^\circ$ would lead to an uncertainty better than ± 5 cm in agreement with estimates from temporal and spatial correlations. Different land cover types show different sensitivities with $11\text{--}15^\circ/10$ cm for open areas and $7\text{--}9^\circ/10$ cm for forested areas. Land classification maps are available and could be used for operational applications. The temperature gradient metamorphosis has to be considered as it biases the CPD toward negative values. In a dense temporal sampling of a few days, a slowly varying background signal would cancel out, such that the estimation of fresh fallen snow would have an accuracy of a few centimeters limited by the phase noise. No evidence was found that soil freezing has a strong influence on the phase difference, but this effect should be studied further. To keep a good estimate for a coarser temporal sampling, meteorological simulations could provide air temperature data and possibly the time of snowfall as an input for physical snow pack models to estimate the temporal evolution of the CPD and to interpolate a coarser sampling rate. However, without any model—except the empirical regression—the RMSE for SD changes was better than ± 3 cm for a sampling rate of 11 days. According to the model, the sensitivity depends linear on frequency such that higher frequencies would allow better accuracies as long as no phase wraps occur. C-band would be at the lower limit, which still could provide a reasonable sensitivity. Frequencies higher than X-band might be good candidates for backscatter measurements, but within the context of this paper, they are promising candidates with a high sensitivity to fresh snow by measuring the CPD. The proposed method to determine the depth of fresh snow is limited to dry snow, when microwaves can penetrate the snow volume. It is a complementary method to wet snow detection algorithms and could fill the current gap of dry snow detection methods.

For future campaigns, experiments on all scales are suggested. Sampling a few square kilometers large areas with a spatial resolution below 30 m would provide the necessary ground measurements for comparison with satellite data. It would be of high interest to measure the alignment and anisotropy of snow grains along snow profiles although this is a challenging task.

Ground-based experiments, which measure the CPD with a high temporal resolution, would add good knowledge to the understanding of the interaction between snow and microwaves, as snow properties could be sampled within the close proximity of the sensor and no extended ground campaigns would be required. Laboratory experiment with snow samples, where the microstructure, the thermal conductivity and the polarization-dependent propagation speed of microwaves at various frequencies are measures could help, to further understand the proposed relationship among mechanical, thermodynamic, and dielectric properties of snow and could stimulate the development of new devices to measure the anisotropy of snow.

ACKNOWLEDGMENT

The authors would like to thank J. Lemmettyinen from FMI for his friendly and very helpful correspondence concerning all presented *in situ* data. Further acknowledgment has to be expressed to J. Pulliaisen, A. Kontu and everybody else from FMI who was involved in the organization and in carrying out the field measurements during the extended ground campaigns in Sodankylae. They would also like to thank the German Aerospace Center (DLR) for providing the large amount of TerraSAR-X and TanDEM-X acquisitions over the test site.

REFERENCES

- [1] M. Schneebeli and S. Sokratov, "Tomography of temperature gradient metamorphism of snow and associated changes in heat conductivity," *Hydrol. Process.*, vol. 18, no. 18, pp. 3655–3665, 2004.
- [2] F. Riche, M. Montagnat, and M. Schneebeli, "Evolution of crystal orientation in snow during temperature gradient metamorphism," *J. Glaciol.*, vol. 59, no. 213, pp. 47–55, 2013.
- [3] M. Sturm and C. Benson, "Scales of spatial heterogeneity for perennial and seasonal snow layers," *Ann. Glaciol.*, vol. 38, no. 1, pp. 253–260, 2004.
- [4] E. Kuusisto, "Snow accumulation and snowmelt in Finland," Publications of the Water Research Institute, National Board of Waters, Helsinki, Finland, No. 55, 1984.
- [5] J. S. Deems, S. R. Fassnacht, and K. J. Elder, "Fractal distribution of snow depth from LiDAR data," *J. Hydrometeorol.*, vol. 7, pp. 285–297, 2006.
- [6] S. C. Colbeck, "The layered character of snow covers," *Rev. Geophys.*, vol. 29, no. 1, pp. 81–96, 1991.
- [7] S. Rasmus, "Spatial and temporal variability of snow bulk density and seasonal snow densification behavior in Finland," *Geophysica*, vol. 49, pp. 53–74, 2013.
- [8] K. J. Bormann, S. Westra, J. P. Evans, and M. F. McCabe, "Spatial and temporal variability in seasonal snow density," *J. Hydrol.*, vol. 484, pp. 63–73, 2013.
- [9] B. R. Pinzer, M. Schneebeli, and T. U. Kaempfer, "Vapor flux and recrystallization during dry snow metamorphism under a steady temperature gradient as observed by time-lapse micro-tomography," *Cryosphere*, vol. 6, no. 5, pp. 1141–1155, 2012.
- [10] F. Ulaby, W. Stiles, L. Dellwig, and B. Hanson, "Experiments on the radar backscatter of snow," *IEEE Trans. Geosci. Electron.*, vol. 15, no. 4, pp. 185–189, Oct. 1977.
- [11] M. Zuniga, T. Habashy, and J. A. Kong, "Active remote sensing of layered random media," *IEEE Trans. Geosci. Electron.*, vol. 17, no. 4, pp. 296–302, Oct. 1979.
- [12] S. Nghiem and W.-Y. Tsai, "Global snow cover monitoring with spaceborne Ku-band scatterometer," *IEEE Trans. Geosci. Remote Sens.*, vol. 39, no. 10, pp. 2118–2134, Oct. 2001.
- [13] S. Yueh *et al.*, "Airborne Ku-band polarimetric radar remote sensing of terrestrial snow cover," *IEEE Trans. Geosci. Remote Sens.*, vol. 47, no. 10, pp. 3347–3364, Oct. 2009.
- [14] S. Pettinato *et al.*, "The potential of COSMO-SkyMed SAR images in monitoring snow cover characteristics," *IEEE Geosci. Remote Sens. Lett.*, vol. 10, no. 1, pp. 9–13, Jan. 2013.

- [15] J. King *et al.*, "UW-Scat: A ground-based dual-frequency scatterometer for observation of snow properties," *IEEE Geosci. Remote Sens. Lett.*, vol. 10, no. 3, pp. 528–532, May 2013.
- [16] X. Xu, L. Tsang, and S. Yueh, "Electromagnetic models of co/cross polarization of bicontinuous/DMRT in radar remote sensing of terrestrial snow at X- and Ku-band for CoReH2O and SCLP applications," *IEEE J. Sel. Topics Appl. Earth Observ. Remote Sens.*, vol. 5, no. 3, pp. 1024–1032, Jun. 2012.
- [17] N. Besic *et al.*, "Dry snow backscattering sensitivity on density change for SWE estimation," in *Proc. IEEE Int. Geosci. Remote Sens. Symp.*, 2012, pp. 4418–4421.
- [18] W. H. Stiles and F. Ulaby, "Dielectric properties of snow," *Remote Sens. Lab.*, Univ. Kansas, Lawrence, KS, USA, RSL Tech. Rep. 527-1, Accession Number ADP000148, pp. 91–103, 1980.
- [19] T. Abe, Y. Yamaguchi, and M. Sengoku, "Experimental study of microwave transmission in snowpack," *IEEE Trans. Geosci. Remote Sens.*, vol. 28, no. 5, pp. 915–921, Sep. 1990.
- [20] W. A. Cumming, "The dielectric properties of ice and snow at 3.2 centimeters," *J. Appl. Phys.*, vol. 23, pp. 768–773, 1952.
- [21] C. Mätzler, "Applications of the interaction of microwaves with the natural snow cover," *Remote Sens. Rev.*, vol. 2, pp. 259–387, 1987.
- [22] J. Shi and J. Dozier, "Radar backscattering response to wet snow," in *Proc. Int. Geosci. Remote Sens. Symp. (IGARSS'92)*, May 1992, vol. 2, pp. 927–929.
- [23] C. Mätzler and E. Schanda, "Snow mapping with active microwave sensors," *Int. J. Remote Sens.*, vol. 5, no. 2, pp. 409–422, 1984.
- [24] J. Koskinen, J. Pullainen, and M. Hallikainen, "The use of ERS-1 SAR data in snow melt monitoring," *IEEE Trans. Geosci. Remote Sens.*, vol. 35, no. 3, pp. 601–610, May 1997.
- [25] T. Nagler and H. Rott, "Retrieval of wet snow by means of multitemporal SAR data," *IEEE Trans. Geosci. Remote Sens.*, vol. 38, no. 2, pp. 754–765, Mar. 2000.
- [26] H. Rott and T. Nagler, "Monitoring temporal dynamics of snowmelt with ERS-1 SAR," in *Proc. Int. Geosci. Remote Sens. Symp. (IGARSS'95)*, Jul. 1995, vol. 3, pp. 1747–1749.
- [27] Snehmani, G. Venkataraman, A. K. Nigam, and G. Singh, "Development of an inversion algorithm for dry snow density estimation and its application with ENVISAT-ASAR dual co-polarization data," *Geocarto Int.*, vol. 25, no. 8, pp. 597–616, 2010.
- [28] P. K. Thakur *et al.*, "Snow physical parameters estimation using space-based synthetic aperture radar," *Geocarto Int.*, vol. 27, no. 3, pp. 263–288, 2012.
- [29] L. Huang *et al.*, "Classification and snow line detection for glacial areas using the polarimetric SAR image," *Remote Sens. Environ.*, vol. 115, no. 7, pp. 1721–1732, 2011.
- [30] L. Ferro-Famil *et al.*, "The potential of full polarimetric SAR data to classify dry snowcover," in *Proc. IEEE Int. Geosci. Remote Sens. Symp. (IGARSS'99)*, 1999, vol. 3, pp. 1792–1794.
- [31] A. Martini *et al.*, "Dry snow extent monitoring in strong topography conditions," in *Proc. IEEE Int. Geosci. Remote Sens. Symp.*, 2005, vol. 8, p. 5440.
- [32] J. Shi, S. Hensley, and J. Dozier, "Mapping snow cover with repeat pass synthetic aperture radar," in *Proc. IEEE Int. Geosci. Remote Sens. Symp. (IGARSS'97)*, Aug. 1997, vol. 2, pp. 628–630.
- [33] G. Singh, G. Venkataraman, Y. S. Rao, and V. Kumar, and Snehmani, "InSAR coherence measurement techniques for snow cover mapping in Himalayan region," in *Proc. IEEE Int. Geosci. Remote Sens. Symp. (IGARSS'08)*, 2008, vol. 4, pp. 1077–1080.
- [34] S. Li and M. Sturm, "Derivation of spatial distribution of snow precipitation using interferometric SAR technique," in *Proc. IEEE Int. Geosci. Remote Sens. Symp. (IGARSS'01)*, 2001, vol. 4, pp. 1795–1797.
- [35] T. Guneriussen, K. A. Høgda, H. Johnsen, and I. Lauknes, "InSAR for estimation of changes in snow water equivalent of dry snow," *IEEE Trans. Geosci. Remote Sens.*, vol. 39, no. 10, pp. 2101–2108, Oct. 2001.
- [36] E. J. Deeb, R. R. Forster, and D. L. Kane, "Monitoring snowpack evolution using interferometric synthetic aperture radar on the North Slope of Alaska," *Int. J. Remote Sens.*, vol. 32, no. 14, pp. 3985–4003, 2011.
- [37] K. Sarabandi and R. Azadegan, "Simulation of interferometric SAR response to rough surfaces covered with a dielectric layer," in *Proc. IEEE Int. Geosci. Remote Sens. Symp. (IGARSS'00)*, 2000, vol. 4, pp. 1739–1741.
- [38] Z. Wang and S. Li, "Detection of winter frost heaving of the active layer of Arctic permafrost using SAR differential interferograms," in *Proc. IEEE Int. Geosci. Remote Sens. Symp. (IGARSS'99)*, 1999, vol. 4, pp. 1946–1948.
- [39] J. Koskinen, "Snow monitoring using interferometric TOPSAR data," in *Proc. IEEE Int. Geosci. Remote Sens. Symp. (IGARSS'01)*, 2001, vol. 6, pp. 2866–2868.
- [40] K. P. Papathanassiou and S. R. Cloude, "Single-baseline polarimetric SAR interferometry," *IEEE Trans. Geosci. Remote Sens.*, vol. 39, no. 11, pp. 2352–2363, Nov. 2001.
- [41] E. Weber Hoen and H. Zebker, "Penetration depths inferred from interferometric volume decorrelation observed over the Greenland ice sheet," *IEEE Trans. Geosci. Remote Sens.*, vol. 38, no. 6, pp. 2571–2583, Nov. 2000.
- [42] A. Ryzhkov and D. Zrnic, "Polarimetric method for ice water content determination," in *Proc. IEEE Int. Geosci. Remote Sens. Symp. (IGARSS'96)*, May 1996, vol. 1, pp. 557–559.
- [43] T. Otto and H. W. J. Russchenberg, "Estimation of specific differential phase and differential backscatter phase from polarimetric weather radar measurements of rain," *IEEE Geosci. Remote Sens. Lett.*, vol. 8, no. 5, pp. 988–992, Sep. 2011.
- [44] P. Chang *et al.*, "Polarimetric backscatter from fresh and metamorphic snowcover at millimeter wavelengths," *IEEE Trans. Antennas Propag.*, vol. 44, no. 1, pp. 58–73, Jan. 1996.
- [45] H. Löwe, F. Riche, and M. Schneebeli, "A general treatment of snow microstructure exemplified by an improved relation for thermal conductivity," *Cryosphere*, vol. 7, no. 5, pp. 1473–1480, 2013.
- [46] J. Lemmettyinen *et al.*, "Technical assistance for the deployment of an X- to Ku-band scatterometer during the NoSREx-III experiment. Final report," ESA ESTEC, Noordwijk, Netherlands, Contract No. 22671/09/NL/JA/ef, Tech. Rep., 2013.
- [47] M. Sturm and J. A. Holmgren, "Self-recording snow depth probe," U.S. Patent 5 864 059, Jan. 1999.
- [48] S. C. Colbeck, "An overview of seasonal snow metamorphism," *Rev. Geophys.*, vol. 20, no. 1, pp. 45–61, 1982.
- [49] M. Sturm and C. S. Benson, "Vapor transport, grain growth and depth-hoar development in the subarctic snow," *J. Glaciol.*, vol. 43, no. 143, pp. 42–59, 1997.
- [50] M. Hallikainen, F. Ulaby, and M. Abdelrazik, "Dielectric properties of snow in the 3 to 37 GHz range," *IEEE Trans. Antennas Propag.*, vol. 34, no. 11, pp. 1329–1340, Nov. 1986.
- [51] A. Wiesmann, C. Mätzler, and T. Weise, "Radiometric and structural measurements of snow samples," *Radio Sci.*, vol. 33, no. 2, pp. 273–289, 1998.
- [52] C. Mätzler and A. Wiesmann, "Extension of the microwave emission model of layered snowpacks to coarse-grained snow," *Remote Sens. Environ.*, vol. 70, no. 3, pp. 317–325, 1999.
- [53] A. Sihvola, "Mixing rules with complex dielectric coefficients," *Subsurf. Sens. Technol. Appl.*, vol. 1, no. 4, pp. 393–415, 2000.
- [54] J.-S. Lee and E. Pottier, *Polarimetric Radar Imaging*. Boca Raton, FL, USA: CRC Press/Taylor & Francis, 2009.
- [55] F. Ulaby, D. Held, M. Donson, K. McDonald, and T. Senior, "Relating polarization phase difference of SAR signals to scene properties," *IEEE Trans. Geosci. Remote Sens.*, vol. GE-25, no. 1, pp. 83–92, Jan. 1987.
- [56] A. Freeman and S. Durden, "A three-component scattering model for polarimetric SAR data," *IEEE Trans. Geosci. Remote Sens.*, vol. 36, no. 3, pp. 963–973, May 1998.
- [57] D. Evans, T. Farr, J. van Zyl, and H. Zebker, "Radar polarimetry: Analysis tools and applications," *IEEE Trans. Geosci. Remote Sens.*, vol. 26, no. 6, pp. 774–789, Nov. 1988.
- [58] R. Alley, "Texture of polar firn for remote sensing," *Ann. Glaciol.*, vol. 9, pp. 1–4, 1987.
- [59] T. Hildebrand, A. Laib, R. Müller, J. Dequeker, and P. Rüeggger, "Direct three-dimensional morphometric analysis of human cancellous bone: Microstructural data from spine, femur, iliac crest, and calcaneus," *J. Bone Miner Res.*, vol. 14, no. 7, pp. 1167–74, Jul. 1999.
- [60] S. Torquato and F. Lado, "Trapping constant, thermal conductivity, and the microstructure of suspensions of oriented spheroids," *J. Chem. Phys.*, vol. 94, no. 6, pp. 4453–4462, 1991.
- [61] R. H. Shertzer and E. E. Adams, "Anisotropic thermal conductivity model for dry snow," *Cold Reg. Sci. Technol.*, vol. 69, no. 2–3, pp. 122–128, 2011.
- [62] G. Parrella, K. Papathanassiou, and I. Hajnsek, "On the interpretation of L- and P-band PolSAR signatures of polythermal glaciers," in *Proc. 6th Int. Workshop Sci. Appl. SAR Polarimetry Polarimetric Interferom. (PolInSAR'13)*, 2013, pp. 1–6.
- [63] O. Levy and D. Stroud, "Maxwell Garnett theory for mixtures of anisotropic inclusions: Application to conducting polymers," *Phys. Rev. B*, vol. 56, pp. 8035–8046, Oct. 1997.
- [64] H. Van De Hulst, *Light Scattering by Small Particles (Structure of Matter Series.)*. New York, NY, USA: Dover, 2010.
- [65] K. Sarabandi, "Derivation of phase statistics from the Mueller matrix," *Radio Sci.*, vol. 27, no. 5, pp. 553–560, 1992.
- [66] Y. Oh, K. Sarabandi, and F. Ulaby, "An empirical model for phase difference statistics of rough surfaces," in *Proc. IEEE Geosci. Remote Sens. Symp. (IGARSS'93)*, 1993, vol. 3, pp. 1003–1005.

- [67] Y. Oh, K. Sarabandi, and F. T. Ulaby, "Semi-empirical model of the ensemble-averaged differential Mueller matrix for microwave backscattering from bare soil surfaces," *IEEE Trans. Geosci. Remote Sens.*, vol. 40, no. 6, pp. 1348–1355, Jun. 2002.
- [68] Y. Lasne *et al.*, "Study of hypersaline deposits and analysis of their signature in airborne and spaceborne SAR data: Example of Death Valley, California," *IEEE Trans. Geosci. Remote Sens.*, vol. 47, no. 8, pp. 2581–2598, Aug. 2009.
- [69] M. Lehning, P. Bartelt, B. Brown, C. Fierz, and P. Satyawali, "A physical SNOWPACK model for the Swiss avalanche warning: Part II. Snow microstructure," *Cold Reg. Sci. Technol.*, vol. 35, no. 3, pp. 147–167, 2002.
- [70] P. Lemke *et al.*, "Observations: Changes in snow, ice and frozen ground," in *Climate Change 2007: The Physical Science Basis. Contribution of Working Group I to the Fourth Assessment Report of the Intergovernmental Panel on Climate Change*, pp. 337–383, 2007.
- [71] M. Rohrer, N. Salzmann, M. Stoffel, and A. V. Kulkarni, "Missing (in-situ) snow cover data hampers climate change and runoff studies in the Greater Himalayas," *Sci. Total Environ.*, vol. 468–469, pp. S60–S70, 2013.
- [72] H.-W. Jacobi, "Snow: A reliable indicator for global warming in the future?," *Environ. Res. Lett.*, vol. 7, no. 1, p. 011004, 2012.
- [73] J. L. Cohen, J. C. Furtado, M. A. Barlow, V. A. Alexeev, and J. E. Cherry, "Arctic warming, increasing snow cover and widespread boreal winter cooling," *Environ. Res. Lett.*, vol. 7, no. 1, p. 014007, 2012.



Silvan Leinss received the Dipl. degree in physics from the University of Constance, Konstanz, Germany, in 2008.

After working in the field of light scattering in colloidal random media at the University of Constance and light scattering statistics in Bose-Einstein Condensates at ETH Zurich he started in 2011 the Ph.D. degree in the field of radar remote sensing and specialized in polarimetric and interferometric approaches for the determination of snow properties. His research interests include electromagnetic scattering properties of ice and snow, radar interferometry, digital elevation models, and efficient implementations of processing algorithms.



Giuseppe Parrella received the Dipl. Ing. degree from the University of Naples Federico II, Naples, Italy, in 2010, and since 2011, he is also Ph.D. student at ETH Zurich, Zürich, Switzerland.

In 2010, he joined the Polarimetric Interferometry Synthetic Aperture Radar (PolInSAR) Research Group, DLR, Wessling, Germany. His research interests include electromagnetic modeling of ice and snow scattering properties, radar polarimetry, and polarimetric interferometry.



Irena Hajnsek (AM'01, M'06, SM'09, FM'14) received the Dipl. degree (Hons.) from the Free University of Berlin, Berlin, Germany, in 1996 and the Dr. degree (Hons.) from the Friedrich Schiller University of Jena, Jena, Germany, in 2001.

Since November 2009, she has been a Professor of Earth Observation, Institute of Environmental Engineering, Swiss Federal Institute of Technology (ETH) Zürich, Zürich, Switzerland, and at the same time, Head of the Polarimetric SAR Interferometry Research Group, Microwaves and Radar Institute, German Aerospace Center, Wessling, Germany. From 1996 to 1999, she was with the Microwaves and Radar Institute (DLR-HF), German Aerospace Center (DLR), Wessling, Germany. From 1999 to 2000, she has been 10 months with the Institut d'Electronique et de Télécommunications de Rennes, University of Rennes 1, France, and 4 months with the Applied Electromagnetics (AEL) in St. Andrews, Scotland, in the frame of the EC-TMR Radar Polarimetry Network. In 2005, she was a Guest Scientist at the University of Adelaide, Adelaide, South Australia, for 6 weeks. She is the Science Coordinator of the German Satellite Mission TanDEM-X. Her research interests include electromagnetic propagation and scattering theory, radar polarimetry, SAR and interferometric SAR data processing techniques, and environmental parameter modeling and estimation.

Dr. Hajnsek was a member of the ESA Mission Advisory Group (MAG) of the 7th Explorer Mission CoReH2O, from 2009 to 2013. She was Technical Program Cochair of the IEEE IGARSS 2012 Symposium in Munich. Since 2013, she has been a member of the IEEE GRSS AdCom.